

Assessment of alternative covariance functions for joint input-state estimation via Gaussian Process latent force models in structural dynamics

S. Vettori^{a,b,*}, E. Di Lorenzo^a, B. Peeters^a and E. Chatzi^b

^aSiemens Digital Industries Software, Interleuvenlaan 68, 3001 Leuven, Belgium

^bInstitute of Structural Engineering, ETH Zürich, Stefano-Franscini-Platz 5, CH-8093 Zürich, Switzerland

ARTICLE INFO

Keywords:

Input-state estimation
Input modeling
Latent Force Model
Gaussian Process
Covariance function

Abstract

Digital technologies can be used to gather accurate information about the behavior of structural components for improving systems design, as well as for enabling advanced Structural Health Monitoring (SHM) strategies. New avenues for achieving automated and continuous structural assessment are opened up via development of virtualization approaches delivering so-called Digital Twins (DTs), i.e., digital mirrored representations of physical systems relying on fusion of simulation models and real-time monitoring data. In this framework, the main motivation of the work presented in this paper stems from the existing challenges in the implementation and deployment of a real-time predictive framework for virtualization of dynamic systems. Kalman-based filters are usually employed in this context to address the task of joint input-state prediction in structural dynamics. A Gaussian Process Latent Force Model (GPLFM) approach is exploited in this work to construct flexible data-driven a priori models for the unknown inputs, which are then coupled with a combined deterministic-stochastic state-space model of the structural component under study for Kalman-based input-state estimation. The use of Gaussian Process (GP) regression for this task overcomes the limitations of the conventionally adopted random-walk model, thus limiting the necessity of offline user-dependent calibration of this type of data assimilation methods. This paper proposes the use of alternative covariance functions for GP regression in structural dynamics. A theoretical analysis of the GPLFMs linked to the investigated covariance functions is offered. The outcome of this study provides insights into the applicability of each covariance type for GP-based input-state estimation. The proposed framework is validated via an illustrative simulated example, namely a 3 Degrees of Freedom (DOF) system subjected to an array of different loading scenarios. Additionally, the performance of the method is experimentally assessed on the task of joint input-state estimation during testing of a 3D-printed scaled Wind Turbine (WT) blade.

1. Introduction

Design, identification, verification and monitoring comprise primary tasks for effectuating an efficient life-cycle management of structural components. Several challenges render the execution of these tasks non-trivial, relating to system complexity, inaccessibility and further deployment limitations, time and cost constraints, as well as external sources of uncertainty. The process of virtualization offers a strategy for narrowing these uncertainties, by harnessing the fusion of physics-based models with data to build a virtual replica of the physical system; a Digital Twin (DT) [1]. This further allows for generating knowledge beyond the sparse physical sensing locations, by permitting to predict response in "virtual sensor" locations. The main challenge behind the definition of DTs lies in the implementation of reliable methodologies for combining model-based and data-based information to create a predictive tool that can evolve over time. To this end, data assimilation techniques are widely adopted in the structural dynamics context for implementation of Virtual Sensing (VS) strategies, i.e., for inferring Quantities of Interest (QoI) such as system responses and/or unknown loads in a dynamic environment [2–13]. The working principle of these strategies relies on use of data for reducing the uncertainties arising from the limitations of mechanistic modeling, which is in turn exploited to expand the available data and gain further knowledge of the system dynamic behavior. Despite VS methods

*Corresponding author

✉ silvia.vettori@siemens.com (S. Vettori); emilio.dilorenzo@siemens.com (E. Di Lorenzo); bart.peeters@siemens.com (B. Peeters); chatzi@ibk.baug.ethz.ch (E. Chatzi)
ORCID(s): 0000-0001-6097-4278 (S. Vettori)

nowadays being recognized as powerful tools for twinning of dynamic systems, several limitations are still to be addressed for improvement of the accuracy and efficiency of the underlying data assimilation process.

Kalman-type filters have been widely exploited in the recent years for constructing virtual sensors [14–19] in linear or even nonlinear contexts [20–22]. Several adaptations of the standard Kalman Filter (KF) algorithm have been constructed to simultaneously address response prediction and inverse load identification of linear dynamic systems in a stochastic setting. To this end, a random-walk equation is commonly adopted as prior assumption on the unknown input dynamics. The resulting equation is then used in combination with the mechanistic stochastic state-space model of the structure, for simultaneously estimating its responses at unmeasured locations and the loads it is subjected to. For instance, within the so-called Augmented Kalman Filter (AKF) algorithm, the random-walk assumption allows to include the unknown input term within a new augmented state vector. The AKF and its applicability to structural dynamics have been proposed in [23]. In [6], the un-observability of the augmented system matrix appearing when only acceleration measurements are considered has been proved and tackled by means of dummy displacement measurements. Alternatively, the numerical issues due to un-observability exhibited by the AKF can be overcome by adopting the so-called Dual Kalman Filter (DKF) for joint input-state estimation. This Kalman-based recursive estimator, presented in [24] and tested in [7], recasts the input and state prediction equations into two sequential stages. Several additional algorithms have been proposed for joint input-state estimation with a time-delayed scheme [25–27]. It has been proven in [27] that these approaches, classified as smoothing schemes, allow to significantly reduce the estimation uncertainty due to measurement noise when measurements collocated with the estimated forces are not available. The challenges derived from instantaneous system inversion for load identification within input-state estimation algorithms have been investigated in [28], where the requirements in terms of sensors quantity and type are investigated. In this sense, an Optimal Sensor Placement (OSP) strategy has been developed in [29, 30] for input-state estimation using the AKF, while a more extended framework based on information theory is proposed in [31–33]. Although the random-walk model and its adaptations are widely adopted as prior input information in generic scenarios when applying joint input-state estimation schemes, this is often not representative of the actual loading conditions. Indeed, the random-walk model can be treated as a special first order autoregressive process with unit root, i.e., a non-stationary process [14], thus resulting in a too strict simplification for loads which deviate from the popular ambient noise excitation scheme. This leads to challenging tuning efforts of the estimators and difficulties in providing reliable loading predictions in generic circumstances. To this end, a more generic model for the input, i.e., a first order stationary autoregressive process, has been used in [14] to address joint input-state-parameter estimation via a combination of the DKF and the Unscented Kalman Filter (UKF) [34–37]. Machine Learning (ML) approaches such as Gaussian Process (GP) regression [38] have been also exploited to construct more comprehensive models for the unknown input. A state-space representation for GP models has been proposed in [39, 40], where a recursive regression solution has been implemented using a combination of Kalman filtering and smoothing. The sequential GP regression solution has been used to construct Gaussian Process Latent Force Models (GPLFMs) with applications in several domains [41–43]. In [44], GPLFMs have been introduced as flexible alternatives for unknown input modeling in the framework of joint input-state estimation of structures. With this purpose, a GPLFM with a Matérn kernel is used in combination with the deterministic-stochastic state-space model of the system for joint input-state prediction via Kalman filtering and smoothing. Besides its higher flexibility, it has been demonstrated in [44] that this method overcomes the un-observability issues arising from the use of the AKF with acceleration-only data sets. The GPLFM has been validated for in-situ measurements in [45], further exploited for input-state-parameter estimation in [46] and adapted for identification of mechanical systems with discontinuous nonlinearity in [47]. Additionally, GP regression has been implemented in both time and space dimensions for recursive distributed load prediction in [48].

A critical review on the necessary tools for building a state-space representation of a GP is presented in this paper. Specifically, a detailed analysis of conventional and non-conventional GP covariance functions in structural dynamics is offered, along with the derivation of their Stochastic Differential Equation (SDE) representations. The latter has been analyzed by means of an analogy with the harmonic oscillators theory, which has served to identify the inner dynamic features of each investigated covariance function. This work proposes the use of bespoke covariance functions according to the analyzed experimental case study in order to maximize the joint input-state estimation performance. To this end, the theoretical study has been complemented with a simulated example concerning a 3 Degrees of Freedom (DOF) system subjected to several loading conditions. The outcome is also experimentally validated on the case study of a 3D-printed scaled Wind Turbine (WT) blade undergoing dynamic testing in clamped-free conditions.

The paper is organized as follows. Section 2 offers the formulation for the Model Order Reduction (MOR) technique adopted in this work, along with a description of the combined deterministic-stochastic state-space equations for a

linear structural system. Section 2 continues by proposing the theoretical background on GP regression and providing a thorough analysis of both conventional and non-conventional kernels (covariance functions) in the structural dynamics context. Section 3 reports on the state-space formulation for recursive GP regression and investigates its features as a function of the adopted kernel by means of an analogy with harmonic oscillators. The construction of Latent Force Models (LFMs) for joint input-state estimation is then presented in Section 4, where some considerations regarding the practical implementation of the method are highlighted. Following the reported notions, a GPLFM framework is built and tested in Section 4 for a 3 DOFs system. An experimental case study is provided in Section 5, where the novel bespoke kernel selection for GP-based input-state estimation is assessed during testing of a 3D-printed scaled WT blade. Finally, the work is concluded in Section 6.

2. Theoretical background

2.1. Bayesian dynamic model of a structural system

The Equation of Motion (EoM) of a linear structural system can be formulated as a second order vector differential equation of the form:

$$\mathbf{M}\ddot{\mathbf{z}}(t) + \mathbf{D}\dot{\mathbf{z}}(t) + \mathbf{K}\mathbf{z}(t) = \mathbf{S}_i\mathbf{u}(t) \quad (1)$$

where $\mathbf{z}(t) \in \mathbb{R}^{n_{dof}}$ is the vector of displacements, usually corresponding to the Finite Element (FE) model DOFs, $\mathbf{M} \in \mathbb{R}^{n_{dof} \times n_{dof}}$, $\mathbf{D} \in \mathbb{R}^{n_{dof} \times n_{dof}}$ and $\mathbf{K} \in \mathbb{R}^{n_{dof} \times n_{dof}}$ denote the mass, damping and stiffness matrices respectively; $\mathbf{u}(t) \in \mathbb{R}^{n_i}$ (with n_i representing the number of loads) is the input vector and $\mathbf{S}_i \in \mathbb{R}^{n_{dof} \times n_i}$ is the Boolean input shape matrix that selects the DOFs where loads (inputs) are applied. A MOR technique [49] can be applied to reduce the model size by formulating the dynamic behavior of a structure as a superposition of modal contributions:

$$\mathbf{z}(t) \approx \mathbf{\Psi}\mathbf{p}(t) \quad (2)$$

where $\mathbf{\Psi} \in \mathbb{R}^{n_{dof} \times n_r}$ is the reduction basis and $\mathbf{p} \in \mathbb{R}^{n_r}$ is the vector of the generalized coordinates of the system, with n_r being the dimension of the reduced coordinates. Inserting the reduction basis into Eq. 1 and premultiplying each term by $\mathbf{\Psi}^T$, the resulting equation is of the form:

$$\mathbf{M}_r\ddot{\mathbf{p}}(t) + \mathbf{D}_r\dot{\mathbf{p}}(t) + \mathbf{K}_r\mathbf{p}(t) = \mathbf{S}_r\mathbf{u}(t) \quad (3)$$

where the mass, damping, stiffness and input shape matrices of the reduced system are respectively $\mathbf{M}_r = \mathbf{\Psi}^T\mathbf{M}\mathbf{\Psi}$, $\mathbf{D}_r = \mathbf{\Psi}^T\mathbf{D}\mathbf{\Psi}$, $\mathbf{K}_r = \mathbf{\Psi}^T\mathbf{K}\mathbf{\Psi}$ and $\mathbf{S}_r = \mathbf{\Psi}^T\mathbf{S}_i$.

The reduction basis adopted in this work is expressed as:

$$\mathbf{\Psi} = [\mathbf{\Psi}_n \quad \mathbf{\Psi}_\alpha] \quad (4)$$

where $\mathbf{\Psi}_n \in \mathbb{R}^{n_{dof} \times n_k}$ is the matrix of the numerical normal modes to be included in the Reduced Order Model (ROM), i.e., the eigenmodes of the entire structure in the frequency range of interest, and $\mathbf{\Psi}_\alpha \in \mathbb{R}^{n_{dof} \times n_\alpha}$ is the residual attachment modes matrix [49, 50], with $n_k + n_\alpha = n_r$.

In the structural dynamics context, it is common practice to transform Eq. 1 into a state-space model [50]. In this work, the use of a combined deterministic-stochastic state-space model is introduced for consistency with the Bayesian approach hereby adopted for the task of input-state estimation. This type of models assume the evolution of states over time to follow a stochastic process with Gaussian errors modeling uncertainties on both the transition and observation equations. The discrete-time version of a structural combined deterministic-stochastic state-space model is of the type:

$$\begin{cases} \mathbf{x}_k = \mathbf{A}_d\mathbf{x}_{k-1} + \mathbf{B}_d\mathbf{u}_{k-1} + \mathbf{w}_{k-1} \\ \mathbf{y}_k = \mathbf{C}\mathbf{x}_k + \mathbf{G}\mathbf{u}_k + \mathbf{v}_k. \end{cases} \quad (5)$$

where the state vector $\mathbf{x}_k = [\mathbf{p}_k^T \quad \dot{\mathbf{p}}_k^T]^T \in \mathbb{R}^{2n_r}$ is described by a Gaussian distribution with mean $\hat{\mathbf{x}}_k \in \mathbb{R}^{2n_r}$ and covariance matrix $\mathbf{P}_k \in \mathbb{R}^{2n_r \times 2n_r}$. Stationary zero-mean uncorrelated white noises \mathbf{w}_k and \mathbf{v}_k have been introduced to

respectively take into account model uncertainties and measurement noise. The covariance matrices associated to \mathbf{v}_k and \mathbf{w}_k are respectively denoted as $\mathbf{R} \in \mathbb{R}^{n_o \times n_o}$ and $\mathbf{Q} \in \mathbb{R}^{2n_r \times 2n_r}$ such that:

$$\mathbb{E} \left\{ \begin{pmatrix} \mathbf{w}_k \\ \mathbf{v}_k \end{pmatrix} \begin{pmatrix} \mathbf{w}_l^T & \mathbf{v}_l^T \end{pmatrix} \right\} = \begin{bmatrix} \mathbf{Q} & \mathbf{0} \\ \mathbf{0}^T & \mathbf{R} \end{bmatrix} \delta_{kl} \quad (6)$$

where δ_{kl} is the Kronecker delta function and the autocovariance terms \mathbf{Q} and \mathbf{R} represent the covariance matrices of \mathbf{w}_k and \mathbf{v}_k , respectively. In Eq. 6, the mutual correlation of these processes has been discarded for simplicity, i.e., the matrix off-diagonal terms are null. Additionally, further simplification is introduced in Eq. 5 via the assumption of uncorrelated process noise sources, i.e. diagonal \mathbf{Q} , and uncorrelated measurement noise sources, i.e., diagonal \mathbf{R} .

2.2. Gaussian Process regression

Regression is a well-known approach for generating models via a data-driven paradigm; given labeled training data sampled independently, regression algorithms learn about the latent data input-output relationships. The simplest approach consists in assuming a linear relationship between outputs and inputs of the underlying function [51–55]. However, this assumption is not always suitable for real-life problems, for which often outputs cannot be computed as a linear combination of inputs. A method to add flexibility to regression consists in assuming distributions over functions modeled via stochastic processes, i.e., collections of random variables [56, 57]. In particular, a GP is a stochastic process for which any finite number of variables have a joint Gaussian distribution [38]. Given an independent variable $t \in \mathbb{R}^d$ and a dependent variable $f(t) : \mathbb{R}^d \rightarrow \mathbb{R}$, a GP is defined as:

$$f(t) \sim \mathcal{GP}(\mu(t), k(t, t', \theta)) \quad (7)$$

where $\mu(t) = \mathbb{E}[f(t)]$ and $k(t, t', \theta) = \mathbb{E}[(f(t) - \mu(t))(f(t') - \mu(t'))]$ are respectively its mean and covariance function, while θ denotes the hyperparameters of the covariance function (see Subsection 2.3 for examples). Since this work will treat signals, which evolve in time domain, it is convenient to introduce the definition of a one-dimensional zero-mean GP:

$$f(t) \sim \mathcal{GP}(0, k(t, t', \theta)) \quad (8)$$

where $t \in \mathbb{R}$. The zero mean assumption allows to simplify the notation without loss of generality, since a realization of a GP with a non-zero mean function can be retrieved from a function drawn from a zero-mean GP with the same covariance by adding the mean function.

Given a training data set of n observations $D = \{\{\tilde{t}_1, \tilde{y}_1\}, \{\tilde{t}_2, \tilde{y}_2\}, \dots, \{\tilde{t}_n, \tilde{y}_n\}\}$ and a GP mean (conventionally 0) and covariance prior, GP regression consists in obtaining the latent function $f(t)$ at unobserved test points such that:

$$y_k = f(t_k) + \varepsilon_k \quad (9)$$

where $\varepsilon_k \sim \mathcal{N}(0, \sigma_n^2)$ is white Gaussian noise corrupting the data. The GP posterior, i.e., the distribution of the latent function at the unobserved locations given the n data points available in D , is a Gaussian distribution with mean and covariance of the following closed-form:

$$\begin{aligned} \hat{\boldsymbol{\mu}} &= \mathbf{K}_{\mathbf{t}, \mathbf{t}}^T (\mathbf{K}_{\tilde{\mathbf{t}}, \tilde{\mathbf{t}}} + \sigma_n^2 \mathbf{I})^{-1} \tilde{\mathbf{y}}; \\ \hat{\mathbf{K}} &= \mathbf{K}_{\mathbf{t}, \mathbf{t}} - \mathbf{K}_{\mathbf{t}, \tilde{\mathbf{t}}}^T (\mathbf{K}_{\tilde{\mathbf{t}}, \tilde{\mathbf{t}}} + \sigma_n^2 \mathbf{I})^{-1} \mathbf{K}_{\tilde{\mathbf{t}}, \mathbf{t}} \end{aligned} \quad (10)$$

where $\tilde{\mathbf{t}} = [\tilde{t}_1, \dots, \tilde{t}_n]^T$ is the vector of observed time points, $\tilde{\mathbf{y}} = [\tilde{y}_1, \dots, \tilde{y}_n]^T$ is the vector of observations, $\mathbf{K}_{\tilde{\mathbf{t}}, \tilde{\mathbf{t}}}$ is the covariance matrix between the observations in D , $\mathbf{K}_{\mathbf{t}, \mathbf{t}}$ is the covariance matrix between the unobserved test points and $\mathbf{K}_{\tilde{\mathbf{t}}, \mathbf{t}}$ is the covariance matrix between the observations and the unobserved test points. Equation 10 is obtained following Bayes' rule by conditioning the joint Gaussian distribution on the observations $\tilde{\mathbf{y}}$ in D and exploiting the properties of multivariate Gaussian distributions [38]. The posterior computation features a computational cost that scales with $O(n^3)$ because of the term $(\mathbf{K}_{\tilde{\mathbf{t}}, \tilde{\mathbf{t}}} + \sigma_n^2 \mathbf{I})^{-1}$.

An important step in the use of GPs for prediction consists in the selection of the prior model to be employed for regression given a set of available measurements. Model selection can be viewed as the set of a priori decisions taken to configure the regression model, e.g., the choice of the covariance form and the selection of its hyperparameters θ , so

defined since they are parameters of a non-parametric model. Indeed, a GP is a function that does not depend on fixed parameters since its parameters increase as soon as new data is available [38]. While the covariance function choice is essentially performed by the user, which can rely on any available prior knowledge regarding the nature of the analyzed data, the selection of hyperparameters, whose nature depends on the chosen type of function (see Subsection 2.3), needs to be performed via tailored algorithms based on a training data set. In this work, the hyperparameter selection is succeeded by maximizing the marginal likelihood [38, 44], i.e., maximizing the probability of the data given the model, w.r.t the hyperparameters. Following this method, values of the covariance hyperparameters are chosen such that the likelihood of the data is maximized when marginalizing, i.e., averaging, over all the possible GP realizations for the chosen covariance function. This method is particularly useful for GPs, since the marginal likelihood computed exploiting the properties of multivariate Gaussian distributions features a simple and analytically tractable expression [38]. The resulting optimization problem is reported in Eq. 11, where maximization of the marginal likelihood has been converted into minimization of the negative logarithmic marginal likelihood for practicality:

$$\underset{\theta}{\operatorname{argmin}} -\log p(\mathbf{y}|\theta) = \underset{\theta}{\operatorname{argmin}} \frac{n}{2} \log 2\pi + \frac{1}{2} \log |\mathbf{K} + \sigma_n^2 \mathbf{I}| + \frac{1}{2} \mathbf{y}^T (\mathbf{K} + \sigma_n^2 \mathbf{I})^{-1} \mathbf{y}. \quad (11)$$

For solving the optimization problem in a GP regression setting, gradient-based optimization is widely exploited since derivatives of Eq. 11 can be easily computed. This class of methods can easily face entrapment in local minima when the adopted cost function is non-convex. As a result, different initial guess on the hyperparameters may be tested to avoid deterioration of the training outcome. With regards to computational complexity, the computation of derivatives implies a flop count of $O(n^2)$ per hyperparameter (if n is the number of data points, then the dimension of the covariance matrix is $n \times n$). Therefore, the most substantial contribution is provided by the inversion of the positive definite covariance matrix, which scales cubically with n .

2.3. Covariance functions for regression via GPs

The covariance function is a key tool for regression via GPs since it embeds any prior knowledge about the sought-after latent function. Validity of covariance functions within the context of GP-theory is subject to certain specifications. An arbitrary time-domain function k of input pairs t and t' is a valid covariance (kernel) function if it satisfies the symmetry and positive semi-definiteness properties [38]. Valid covariance functions can be manipulated to construct more complex versions by exploiting composition rules, e.g., sum, product, scaling rules [38].

2.3.1. Conventional covariance functions in structural dynamics

Isotropic covariance functions are commonly adopted for regression via GPs in the structural dynamics context. The most common types of covariance functions are reported below for time-domain one-dimensional GPs.

Squared exponential covariance function:

$$k(\tau) = \sigma^2 \exp\left(-\frac{\tau^2}{2l^2}\right), \quad \tau = |t - t'| \quad (12)$$

where l is the characteristic length-scale controlling the bandwidth of the resulting process and σ is the signal variance controlling the magnitude of the process. This covariance function is infinitely differentiable, which implies infinite mean square differentiability of the GP with a squared exponential covariance function. The latter has therefore a very smooth shape.

Exponential covariance function:

$$k(\tau) = \sigma^2 \exp\left(-\frac{\tau}{2l}\right), \quad \tau = |t - t'| \quad (13)$$

where l is the characteristic length-scale and σ is the magnitude-scale. This type of functions generate mean square continuous but not mean square differentiable GPs, which thus have a non-smooth shape.

Matérn covariance function:

$$k(\tau; \nu, \sigma, l) = \sigma^2 \frac{2^{1-\nu}}{\Gamma(\nu)} \left(\frac{\sqrt{2\nu}}{l} \tau \right)^\nu K_\nu \left(\frac{\sqrt{2\nu}}{l} \tau \right), \quad \tau = |t - t'| \quad (14)$$

where l is the length-scale hyperparameter, σ is the magnitude-scale hyperparameter, ν is the smoothness parameter, $\Gamma(\nu)$ is the Gamma function and K_ν is a modified Bessel function of second kind [58]. For half-integer values of ν , i.e., non-negative integer values of $p = \nu - \frac{1}{2}$, the covariance function can be written as the product of a decaying exponential and a polynomial of order p [58]:

$$k_{\nu=p+1/2} = \sigma^2 \exp\left(\frac{-\sqrt{2\nu}\tau}{l}\right) \frac{\Gamma(p+1)}{\Gamma(2p+1)} \sum_{i=0}^p \frac{(p+i)!}{i!(p-1)!} \left(\frac{\sqrt{8\nu}\tau}{l}\right)^{p-i}. \quad (15)$$

The smoothness parameter ν determines the decaying rate of the covariance function, its differentiability and the mean square differentiability of the corresponding GP. For $p = 0$ ($\nu = 0.5$), the Matérn covariance function corresponds to an exponential covariance function, i.e., it is continuous but not differentiable. For $\nu \rightarrow \infty$, the function converges to a squared exponential covariance function, i.e., it is infinitely differentiable. More generally, Matérn covariance functions generate GPs that are $\nu - 1$ times mean square differentiable [38]. These concepts are visually demonstrated by Fig. 1, which displays Matérn covariance functions with assigned l and σ for different ν values (left) and corresponding random GP realizations (right). Figure 1 reports the square exponential and the exponential covariance functions as limit cases for the Matérn class, respectively achieved for $\nu = 0.5$ and $\nu \rightarrow \infty$. Additionally, Fig. 1 provides a visible insight regarding the functions differentiability scaling with ν .

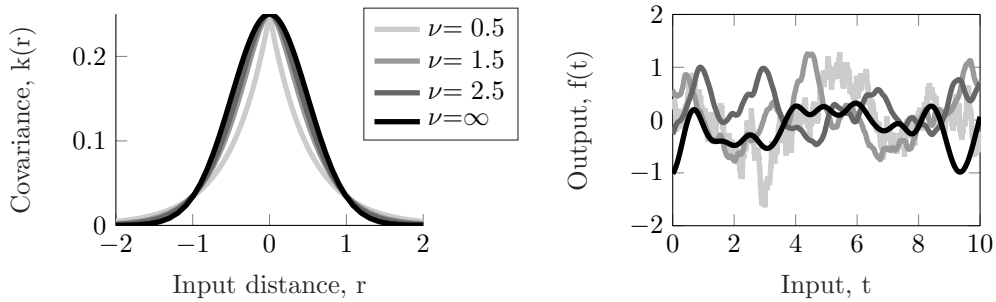


Figure 1: Matérn covariance functions with $\sigma = l = 0.5$ as a function of the input distance $r = t - t'$, for different values of ν (left). Realizations drawn from GPs with Matérn covariance functions ($\sigma = l = 0.5$) for different values of ν (right).

2.3.2. Alternative covariance functions in structural dynamics

The previously presented covariance functions are the most commonly employed for GP regression in the structural dynamics context. In this section, several alternative covariance functions are extensively described.

Periodic covariance functions

Periodic stationary covariance functions can be derived via the so-called warping method, i.e., introducing a periodic mapping $u(t)$ of the input t and using a stationary covariance function in the u space [59]. A typical choice for the periodic function is $u = (\sin(t), \cos(t))^T$, for which the following stationary property holds:

$$\|u(t) - u(t')\|^2 = (\sin(t) - \sin(t'))^2 + (\cos(t) - \cos(t'))^2 + 4\sin^2\left(\frac{t-t'}{2}\right). \quad (16)$$

A commonly adopted periodic covariance function is the so-called canonical periodic covariance function, which is derived as a squared exponential covariance in the previously introduced u space:

$$k(\tau; \sigma, l, \omega_0) = \sigma^2 \exp \left(-\frac{2 \sin^2 \left(\frac{\omega_0 \tau}{2} \right)}{l^2} \right) \quad (17)$$

where $\tau = |t - t'|$, l is the length-scale hyperparameter, σ the magnitude-scale hyperparameter and ω_0 the frequency. It is common practice to refer to the period length parameter, i.e., $t_{period} = 2\pi/\omega_0$, rather than the frequency. Figure 2 illustrates a representation of the canonical periodic covariance function (left) and corresponding GP realization at several values of t_{period} .

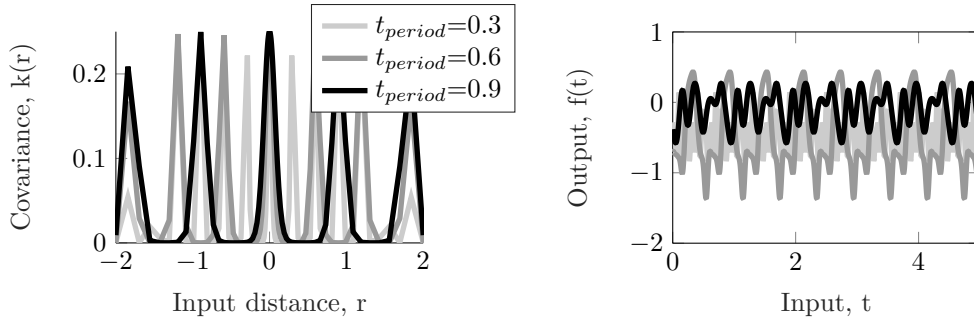


Figure 2: Periodic covariance functions with $\sigma = l = 0.5$ as a function of the input distance $r = t - t'$, for different values of t_{period} (left). Realizations drawn from GPs with periodic covariance functions ($\sigma = l = 0.5$) for different values of t_{period} (right).

Quasiperiodic covariance functions

In practical applications, using a periodic covariance function may result in a too strict assumption. To account for variability effects, a quasiperiodic covariance function can be adopted. This type of covariance function is obtained from the product of a periodic covariance function and a covariance function with long characteristic length scale, i.e., Matérn covariance functions. This feature allows for the introduction of a slow decay effect, i.e., damping effect, which is controlled by the smoothness parameter of the Matérn covariance function as described in Fig. 1. Figure 3 (left) shows a representation of a quasiperiodic covariance function obtained from the product of a canonical periodic function and a squared exponential covariance function (Matérn with $\nu \rightarrow \infty$) for several values of t_{period} . The relative GP realizations are reported in Figure 3 (right). The visual information provided by Fig. 3 proves that the quasiperiodic covariance function is a damped version (with damping dependent on the smoothness of the Matérn covariance function) of the periodic covariance function.

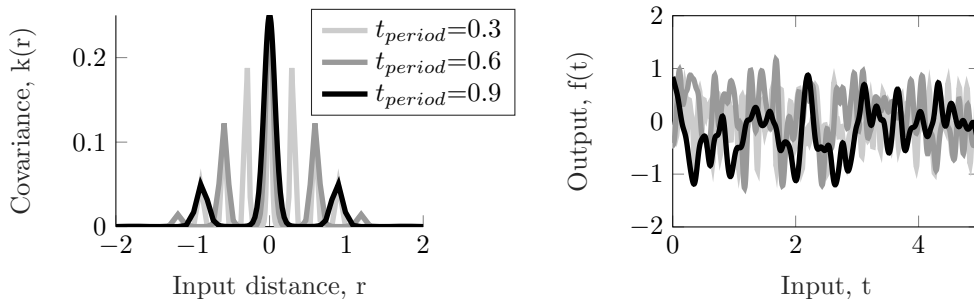


Figure 3: Quasiperiodic covariance functions with $\sigma_{per} = l_{per} = \sigma_{se} = l_{se} = 0.5$ as a function of the input distance $r = t - t'$, for different values of t_{period} (left). Realizations drawn from GPs with periodic covariance functions ($\sigma_{per} = l_{per} = \sigma_{se} = l_{se} = 0.5$) for different values of t_{period} (right).

Constant covariance functions

Constant covariance functions are conventionally adopted to model biases in GPs. A constant covariance function is defined as:

$$k(t, t') = \sigma^2 \quad (18)$$

where σ is the magnitude-scale hyperparameter. Figure 4 depicts constant covariance functions and relative GP realizations for several values of the magnitude scale hyperparameter.

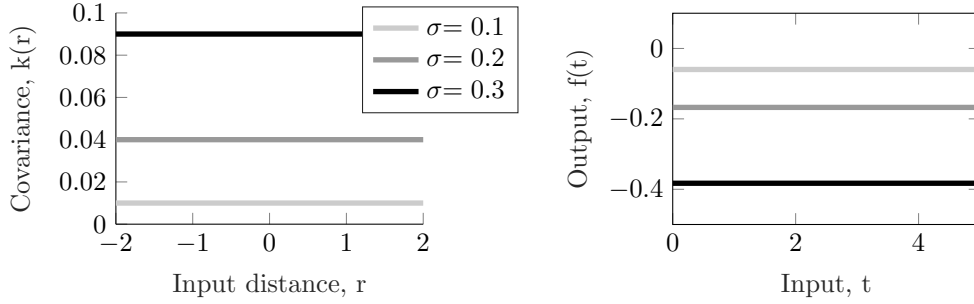


Figure 4: Constant covariance functions as a function of the input distance $r = t - t'$, for different values of σ (left). Realizations drawn from GPs with constant covariance functions for different values of σ (right).

Biased quasiperiodic covariance functions

A biased quasiperiodic covariance function is obtained from a constant and a quasiperiodic covariance function as:

$$k = k_{constant} + k_{quasiperiodic} \quad (19)$$

The sum rule is thus exploited to build a more complex covariance function in which a constant offset is added on top of the dynamics, which are fully modeled via the quasiperiodic function. This operation is commonly adopted in regression problems where data are distributed around a bias, which would not be detected without the introduction of a static term via the constant covariance function. A visualization of the biased quasiperiodic covariance function for several values of the constant covariance magnitude-scale is reported in Fig. 5 (left), while Fig. 5 (right) displays the respective GP realizations.

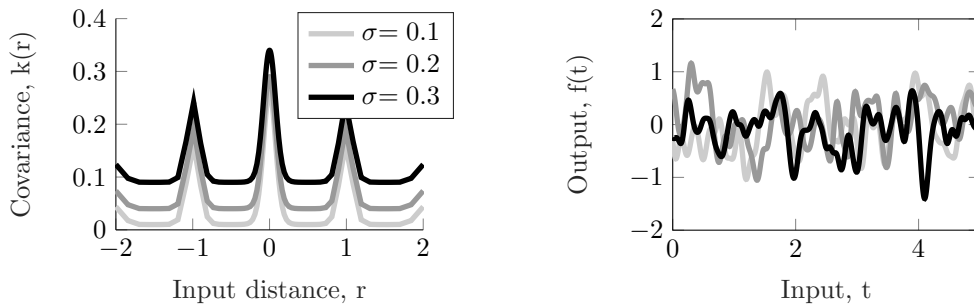


Figure 5: Biased quasiperiodic covariance functions as a function of the input distance $r = t - t'$, for different values of $\sigma_{constant}$ (left). Realizations drawn from GPs with biased quasiperiodic covariance functions for different values of $\sigma_{constant}$ (right).

Linear covariance functions

Linear covariance functions can be adopted for regression via GPs to model linear trends in data. A linear covariance function is defined as:

$$k(t, t') = \sigma^2 t t' \quad (20)$$

where σ is the magnitude-scale hyperparameter. Figure 6 illustrates linear covariance functions and relative GP realizations for several values of the magnitude-scale hyperparameter.

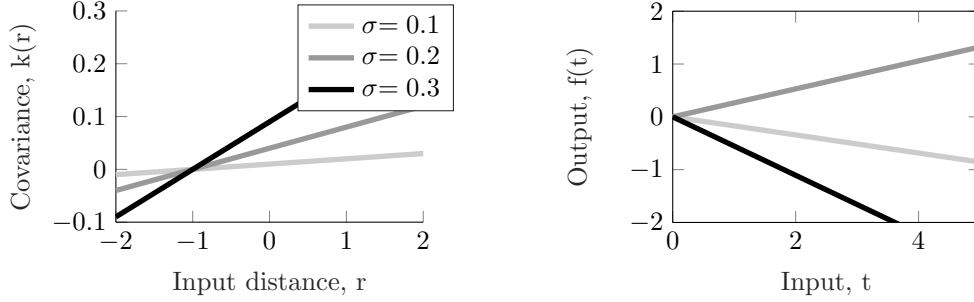


Figure 6: Linear covariance functions as a function of the input distance $r = t - t'$, for different values of σ (left). Realizations drawn from GPs with linear covariance functions for different values of σ (right).

Wiener covariance functions

The Wiener process, i.e., a pure Brownian motion, is a widely adopted non-stationary process. Its covariance function is defined as:

$$k(t, t') = \sigma^2 \min(t, t') \quad (21)$$

valid for $t, t' \geq 0$, with σ being the magnitude-scale hyperparameter. A representation of the Wiener covariance function and relative GP realizations for several values of σ is provided in Fig. 7. Figure 7 (right) proves that a covariance function such as Eq. 21 generates GP samples that are in the form of random-walk models. In this sense, a GP with a Wiener covariance function is an alternative to the direct random-walk expression adopted for input-state estimation within Kalman-type filters such as the AKF.

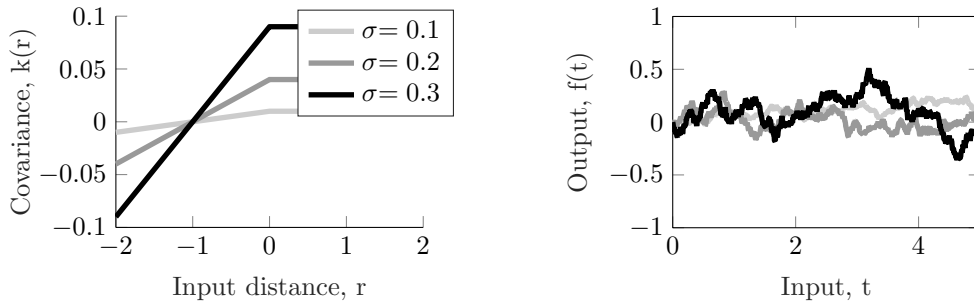


Figure 7: Wiener covariance functions as a function of the input distance $r = t - t'$, for different values of σ (left). Realizations drawn from GPs with Wiener covariance functions for different values of σ (right).

3. Gaussian Process regression in state-space form

The main drawback of the direct solution for regression via GPs (see Eq. 10) consists in the computational complexity scaling as $O(n^3)$, where n in this work corresponds to the number of time instances in the observations

used for regression. In actual monitoring measurements, the collected data is relatively big (and highly sampled), resulting in a large amount of time required for GP regression. To remedy this problem, a sequential inference scheme, whose computational complexity scales linearly with n , can be implemented using Kalman filtering and smoothing [39]. In view of adopting a sequential approach, the GP needs to be formulated as a dynamical system rather than adopting the conventional kernel formalism. This consists in expressing a GP as a solution of the following m^{th} order Linear Time Invariant (LTI) SDE:

$$\frac{d^m f(t)}{dt^m} + a_{m-1} \frac{d^{m-1} f(t)}{dt^{m-1}} + \dots + a_1 \frac{df(t)}{dt} + a_0 f(t) = w(t) \quad (22)$$

where w is a zero-mean continuous-time white noise process. Every solution $f(t)$ of Eq. 22 is a sample function of a GP defined by a certain covariance function k . Collecting the derivative terms in Eq. 22 builds the so-called companion form, i.e., a linear state-space model to be employed in the recursive inference scheme:

$$\begin{cases} \dot{\mathbf{z}}(t) = \mathbf{F}\mathbf{z}(t) + \mathbf{L}w(t) \\ f(t) = \mathbf{H}\mathbf{z}(t) \end{cases} \quad (23)$$

where the input state $\mathbf{z} \in \mathbb{R}^m$ and the matrices $\mathbf{F} \in \mathbb{R}^{m \times m}$, $\mathbf{L} \in \mathbb{R}^{m \times 1}$ and $\mathbf{H} \in \mathbb{R}^{1 \times m}$ are given by:

$$\mathbf{z}(t) = \begin{bmatrix} f(t) \\ \frac{df(t)}{dt} \\ \vdots \\ \frac{d^{m-2}f(t)}{dt^{m-2}} \\ \frac{d^{m-1}f(t)}{dt^{m-1}} \end{bmatrix}, \quad \mathbf{F} = \begin{bmatrix} 0 & 1 & 0 & \dots & 0 \\ 0 & 0 & 1 & \dots & 0 \\ \vdots & \vdots & \vdots & \ddots & \vdots \\ 0 & 0 & 0 & \dots & 1 \\ -a_0 & -a_1 & \dots & \dots & -a_{m-1} \end{bmatrix}, \quad \mathbf{L} = \begin{bmatrix} 0 \\ 0 \\ \vdots \\ 0 \\ 1 \end{bmatrix}, \quad \mathbf{H} = [1 \ 0 \ \dots \ 0 \ 0]. \quad (24)$$

To be employed for GP sequential inference, the first equation in Eq. 23 must be transformed in a discrete-time model of the form:

$$\mathbf{z}_k = \mathbf{F}_{d_{k-1}} \mathbf{z}_{k-1} + \mathbf{q}_{k-1}, \quad \mathbf{q}_{k-1} \sim \mathcal{N}(\mathbf{0}, \mathbf{Q}_{k-1}) \quad (25)$$

where the state transition and process noise covariance matrices can be calculated analytically as:

$$\begin{aligned} \mathbf{F}_{d_{k-1}} &= \exp(\mathbf{F}\Delta t) \\ \mathbf{Q}_{k-1} &= \int_0^{\Delta t} \exp(\mathbf{F}(\Delta t - \tau)) \mathbf{L} \mathbf{q}_c \mathbf{L}^T \exp(\mathbf{F}^T(\Delta t - \tau)) d\tau \end{aligned} \quad (26)$$

where $\Delta t = t_k - t_{k-1}$ [60]. The second equation in Eq. 23 instead represents the intrinsically discrete measurement model, on top of which the noise term ε_k (introduced in Eq. 9) must be added to account for noisy observations:

$$f_k = \mathbf{H}\mathbf{z}_k + \varepsilon_k, \quad \varepsilon_k \sim \mathcal{N}(0, \sigma_n^2). \quad (27)$$

Given the model postulated by Eqs. 25 and 27, GP sequential inference consists in estimating the state vector \mathbf{z}_k at any k given the available measurements for $k = 0 : \Delta t : T$. This operation can be performed in two sequential steps: the filtered posterior distribution of \mathbf{z} is computed via a KF, then a Rauch-Tung-Striebel (RTS) smoother is employed to evaluate the smoothing distribution of \mathbf{z} [39]. Both the KF and the RTS smoother algorithms scale with $O(m^2 n)$ in computational complexity, hence allowing for substantial computational time reduction with respect to the GP regression naive implementation. The same benefit applies for covariance hyperparameters optimization via the minimization of the negative log-likelihood since the marginal likelihood in Eq. 11 can be sequentially evaluated as a by-product of the KF update [61].

The SDE representation of the GP in Eq. 22 is determined by the GP kernel (covariance function). According to the adopted class of covariance function, either an exact LTI state-space SDE representation or an approximated version can be retrieved. A collection of state-space SDE representations for the previously presented covariance functions is reported in the following.

Matèrn class

For GPs with a covariance function of the Matèrn type, an exact state-space representation can be extracted following the rational spectrum approach. The latter derives from the assumption of a rational spectral density for this class of covariance functions. In order to introduce the concept of spectral density, it is convenient to define covariance functions for zero-mean complex-valued GPs: $k(\mathbf{t}, \mathbf{t}') = \mathbb{E} [f(\mathbf{t})f^*(\mathbf{t}')]$ with $\mathbf{t}, \mathbf{t}' \in \mathbb{C}^d$. Bochner's theorem [38, 57, 62] states that a complex-valued function k defined on \mathbb{R}^d is the covariance function of a weakly stationary square continuous complex-valued GP in \mathbb{R}^d if and only if it can be represented as:

$$k(\boldsymbol{\tau}) = \int_{\mathbb{R}^d} e^{2\pi i \mathbf{f} \cdot \boldsymbol{\tau}} \mu(d\mathbf{f}) = \int_{\mathbb{R}^d} e^{2\pi i \mathbf{f} \cdot \boldsymbol{\tau}} dF(\mathbf{f}) \quad (28)$$

where $\boldsymbol{\tau} = \mathbf{t} - \mathbf{t}'$, μ is a positive finite measure and $F(\mathbf{f})$ is defined such that $\mu(d\mathbf{f}) = dF(\mathbf{f})$. If μ is absolutely continuous, then F is differentiable almost everywhere and $\mu(d\mathbf{f}) = S(\mathbf{f})d\mathbf{f}$, where $S(\mathbf{f})$ is defined as the spectral density or power spectrum corresponding to k . Introducing $S(\mathbf{f})$ into Eq. 28 and exploiting Wiener-Khintchine theorem [63], k and $S(\mathbf{f})$ can be defined as Fourier duals:

$$k(\boldsymbol{\tau}) = \int S(\mathbf{f})e^{2\pi i \mathbf{f} \cdot \boldsymbol{\tau}} d\mathbf{f}, \quad S(\mathbf{f}) = \int k(\boldsymbol{\tau})e^{-2\pi i \mathbf{f} \cdot \boldsymbol{\tau}} d\boldsymbol{\tau}. \quad (29)$$

The relationships in Eq. 29 can be expressed for a one-dimensional temporal problem as:

$$k(\tau) = \int S(f)e^{2\pi i f \cdot \tau} df, \quad S(f) = \int k(\tau)e^{-2\pi i f \cdot \tau} d\tau, \quad f = \frac{\omega}{2\pi}. \quad (30)$$

Following Eq. 30, this paragraph will make use of the Fourier Transform (FT) to link time and frequency domains and compute the spectral density for a Matèrn covariance function. In particular, when k falls in the Matèrn class of functions, its FT yields:

$$S(\omega) = \sigma^2 \frac{2\pi^{1/2}\Gamma(\nu + 1/2)}{\Gamma(\nu)} \lambda^{2\nu} (\lambda^2 + \omega^2)^{-(\nu+1/2)}, \quad \lambda = \frac{\sqrt{2\nu}}{l} = \frac{\sqrt{2(p+1)}}{l}. \quad (31)$$

Under the assumption of ν being a half-integer, the spectral density can be reformulated as:

$$S(\omega) = \sigma^2 \frac{2\pi^{1/2}\Gamma(p+1)}{\Gamma(p+1/2)} \lambda^{2p+1} (\lambda^2 + \omega^2)^{-(p+1)}. \quad (32)$$

After grouping all constant terms in a single constant q_c , the spectral density can be factorized in a rational fraction form:

$$S(\omega) = q_c (\lambda^2 + \omega^2)^{-(p+1)} = q_c (\lambda + i\omega)^{-(p+1)} (\lambda - i\omega)^{-(p+1)} = q_c G(i\omega)G(-i\omega). \quad (33)$$

Equation 33 can be interpreted as the spectral density of the output of a system with Transfer Function (TF) $G(i\omega) = (\lambda + i\omega)^{-(p+1)}$, excited by an input $w(t)$ (white noise with spectral density q_c):

$$F(\omega) = G(i\omega)W(\omega). \quad (34)$$

In Eq. 34, $F(\omega)$ (FT of $f(t)$) is the system output with spectral density $S(\omega)$ and $W(\omega)$ is the FT of the exciting term $w(t)$, i.e., $W = \sqrt{(q_c)}$. The function $f(t)$ is the GP with Matèrn covariance function k , i.e., with desired spectral density $S(\omega)$. For the Matèrn class of covariance functions, the TF $G(i\omega)$ has a rational form of the type $G(i\omega) = ((i\omega)^m + a_{m-1}(i\omega)^{m-1} + \dots + a_0)^{-1}$. Hence, Eq. 34 can be reformulated as:

$$F(\omega)[(i\omega)^m + a_{m-1}(i\omega)^{m-1} + \dots + a_0] = W(\omega). \quad (35)$$

The inverse FT of Eq. 35 provides the LTI SDE in Eq. 22, which thus models the evolution in time of sample functions drawn from a GP with covariance k expressed by Eq. 15 [39]. The associated LTI SDE can be easily translated into the

linear state-space model postulated by Eqs. 23 and 24, where the involved coefficients can be determined by analyzing the form of the Matérn covariance functions TF:

$$G(i\omega) = \frac{1}{(\lambda + i\omega)^{p+1}}. \quad (36)$$

For example, Eq. 36 for $\nu = \frac{5}{2}$ ($p = 2$) has the form:

$$G(i\omega) = \frac{1}{(\lambda + i\omega)^3} \quad (37)$$

where the denominator can be rewritten as $\lambda^3 + (i\omega)^3 + 3\lambda^2(i\omega) + 3\lambda(i\omega)^2$. Hence, the coefficients a_m, \dots, a_0 with $m = 3$ are: $a_3 = 1, a_2 = 3\lambda, a_1 = 3\lambda^2, a_0 = \lambda^3$ and the resulting SDE is:

$$\frac{d^3 f(t)}{dt^3} + 3\lambda \frac{d^2 f(t)}{dt^2} + 3\lambda^2 \frac{df(t)}{dt} + \lambda^3 f(t) = w(t). \quad (38)$$

The roots of this SDE are real and coincident with multiplicity equal to 3: $\omega_1 = \omega_2 = \omega_3 = -\lambda$. These correspond to the poles of the system with TF postulated by Eq. 37, whose bode plot is displayed in Fig. 8. The system poles can be computed by setting the denominator of Eq. 37 equal to zero and solving the so-called characteristic equation. This result can be extended to all orders as roots of SDEs associated to Matérn kernels are always equal to $-\lambda$ with multiplicity $p + 1$. Therefore, the system with TF in Eq. 36 is “critically damped” for any integer p , i.e., the time waveform is an exponentially decaying function with a decaying rate driven by the value of $\lambda = \frac{\sqrt{2\nu}}{l} = \frac{\sqrt{2(p+1)}}{l}$. This

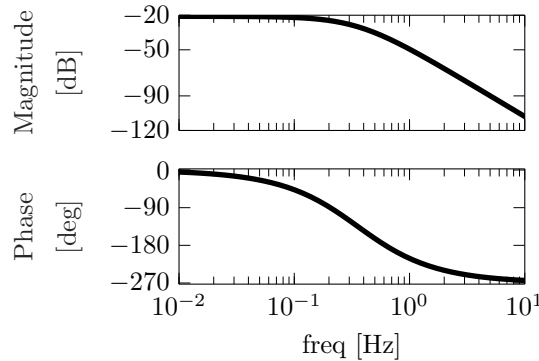


Figure 8: GP with Matérn covariance function: TF of the equivalent SDE system

result is confirmed by the TF shape visible in Fig. 8 for $p = 2$. The higher λ (and ν) is, the faster will be the decay. A mathematical proof to this is provided by the homogeneous solution for Eq. 38, which could only correspond to:

$$g(t) = \tilde{g} e^{-\lambda t} \quad (39)$$

where \tilde{g} can be determined by substituting this expression into the unforced SDE, yielding (for $p = 2$):

$$\frac{d^3 \tilde{g}}{dt^3} e^{-\lambda t} = 0. \quad (40)$$

Since the exponential function never equals 0, the only possible solution for Eq. 40 is given by $\frac{d^3 \tilde{g}}{dt^3} = 0$. This expression can be double integrated to get $\tilde{g} = c_1 + c_2 t + c_3 t^2$. Therefore, the explicit form of Eq. 40 is given by:

$$g = (c_1 + c_2 t + c_3 t^2) e^{-\lambda t} \quad (41)$$

where constants can be determined by applying the initial conditions on $g, \frac{dg}{dt}, \frac{d^2 g}{dt^2}$. This homogeneous solution should be convoluted with the forcing term $w(t)$ to get the forced response of the system with TF $G(i\omega)$: $f(t) = g(t) * w(t)$ [64]. The same result could also be obtained by exploiting partial fraction expansion from control theory to manipulate the TF $G(\omega)$.

Periodic class

A periodic and symmetric covariance function can be expanded into a convergent Fourier series of the form:

$$k(\tau) = \sum_{j=0}^{\infty} q_j^2 \cos(j\omega_0\tau). \quad (42)$$

The spectral density corresponding to Eq. 42 consists of delta peaks at the harmonic frequencies defined by ω_0 , i.e., the angular frequency defining the periodicity of the function:

$$S_p(\omega) = \sum_{j=0}^{\infty} q_j^2 \pi [\delta(\omega - j\omega_0) + \delta(\omega + j\omega_0)]. \quad (43)$$

This spectral density does not exhibit a rational form, thus implying that the procedure adopted for Matérn covariance functions can not be used for building the state-space representation of a GP with a periodic covariance function. However, each j^{th} term in Eq. 42 can be seen as the covariance function of the sum of statistically independent resonators $\sum_{j=0}^{\infty} x_j(t)$ such that:

$$f_j(t) = (x_j(t), y_j(t))^T \quad (44)$$

with the initial condition $f_j(0) \sim \mathcal{N}(0, q_j^2 I)$ and the following differential equations defining the harmonic oscillator:

$$\frac{dx_j(t)}{dt} = -j\omega_0 y_j(t), \quad \frac{dy_j(t)}{dt} = j\omega_0 x_j(t). \quad (45)$$

Solving Eq. 45 yields:

$$x_j(t) = x_j(0)\cos(\omega_0 j t) - y_j(0)\sin(\omega_0 j t) \quad (46)$$

with associated covariance $\mathbb{E}[x_j(t)x_j(t+\tau)] = q_j^2 \cos(j\omega_0\tau)$. As a result, these processes are deterministic with initial state drawn from a Gaussian distribution. The corresponding state-space formulation features block diagonal matrices composed of J matrices as follows:

$$F_j = \begin{bmatrix} 0 & -\omega_0 j \\ \omega_0 j & 0 \end{bmatrix}, \quad L_j = I_2, \quad P_{\infty,j} = q_j^2 I_2, \quad Q_c = 0, \quad H_j = \begin{bmatrix} 1 & 0 \end{bmatrix}. \quad (47)$$

In order to retrieve the form in Eq. 42 for the canonical covariance function in Eq. 17, the relation $2 \sin^2\left(\frac{\tau}{2}\right) = 1 - \cos(\tau)$ must be substituted in the canonical covariance function expression. After expanding the exponential function via a Taylor series, the following expression is obtained:

$$k(\tau) = \exp(-l^2) \sum_{j=0}^{\infty} \frac{1}{j!} \cos^j(\tau). \quad (48)$$

This series can be truncated at an order J and the powers of cosines can be written as summation of cosine terms with multiplied angles. This leads to the following expression for the canonical periodic covariance function:

$$k(\tau) = \sum_{j=0}^J \hat{q}_{j,J}^2 \cos(j\tau) \quad (49)$$

with coefficients $\hat{q}_{j,J}^2 = \frac{2}{\exp(l^2)} \sum_{i=0}^{\lfloor \frac{J-j}{2} \rfloor} \frac{(2l^2)^{-j-2i}}{(j+i)!i!}$, where $j = 1, \dots, J$. An approximation of this expression can be retrieved taking the limit $J \rightarrow \infty$ [59]. The eigenvalues associated to the dynamical system corresponding to a GP with covariance function described by Eq. 49 are complex conjugates with zero real part (each pair corresponds to the eigenvalues associated to the j^{th} component, with the first two eigenvalues being zero). Referring to the single j^{th}

component, a differential equation with imaginary conjugate poles corresponds to an undamped system with frequency specified by the magnitude of the imaginary part. Solving the eigenvalue solution for the reconstructed state-space model yields eigenvalues that are multiples of $\omega_0 = 2\pi/t_{period}$. The solution of the j^{th} differential equation is therefore: $x_j(t) = x_j(0)\cos(\omega_0 jt) - y_j(0)\sin(\omega_0 jt)$, as anticipated in Eq. 46. It follows that the resulting GP will be a summation of J harmonic components (harmonics of ω_0). The latter are visible in Fig. 9, which shows the bode plot of the TF for the dynamical system associated to a GP with canonical periodic covariance function with $\omega_0 = 1$ and truncation order $J = 6$. Figure 9 proves that the TF features a $0Hz$ component and J undamped harmonics (one for each j^{th} component).

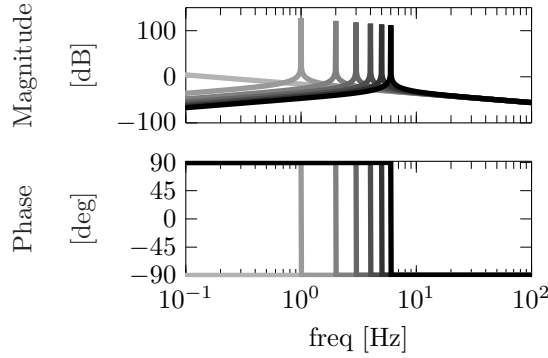


Figure 9: GP with periodic covariance function: TFs of the equivalent SDE system

Quasiperiodic class

Following the kernel product rule, a quasiperiodic covariance function can be constructed as a product of a periodic and a Matérn covariance function. As a result, the Kronecker product can be exploited as follows to build the related state-space model:

$$\begin{aligned} F_j &= F^q \otimes I_2 + I_q \otimes F_j^p, & L_j &= L^q \otimes L_j^p, & Q_{c,j} &= Q_c^q \otimes q_j^2 I_2 \\ P_{\infty,j} &= P_\infty^q \otimes P_{\infty,J}^p, & H_j &= H^q \otimes H_j^p \end{aligned} \quad (50)$$

where the p and q notations are respectively used for matrices associated with the periodic and the Matérn covariance function.

The eigenvalue solution for the system in Eq. 50 provides, for each j^{th} component, complex conjugate pairs of eigenvalues. The dynamical system representing a quasiperiodic covariance function thus corresponds to an underdamped system with solution of the type $x_j(t) = e^{\alpha t}(x_j(0)\cos(\omega_0 jt) - y_j(0)\sin(\omega_0 jt))$. This is confirmed by the bode plot of the TF reported in Fig. 10, which features a $0Hz$ component and J damped harmonics (one for each j^{th} component).

Constant class

A constant covariance function is degenerate and the corresponding state-space model representation is given by the matrices:

$$F = 0, \quad L = 1, \quad Q_c = 0, \quad H = 1, \quad P_0 = \sigma^2. \quad (51)$$

The bode plot for the TF associated with this model is reported in Fig. 11.

Linear class

A linear covariance function is degenerate and the corresponding state-space model is defined by the matrices:

$$F = \begin{bmatrix} 0 & 1 \\ 0 & 0 \end{bmatrix}, \quad L = \begin{bmatrix} 0 \\ 1 \end{bmatrix}, \quad Q_c = 0, \quad H = [1 \ 0], \quad P_0 = \sigma^2 \begin{bmatrix} t_0^2 & t_0 \\ t_0 & 1 \end{bmatrix}. \quad (52)$$

The bode plot for the TF associated with this model coincides with the bode plot related to the constant covariance function (see Fig. 11).

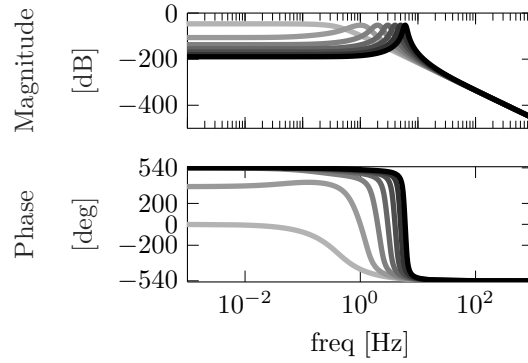


Figure 10: GP with quasiperiodic covariance function: TFs of the equivalent SDE system

Wiener class

The state-space model representation of a Wiener process is defined by the matrices:

$$F = 0, \quad L = 1, \quad Q_c = \sigma^2, \quad H = 1, \quad P_0 = 0. \quad (53)$$

The bode plot for the TF associated with this model coincides with the bode plot related to the constant covariance function (see Fig. 11).

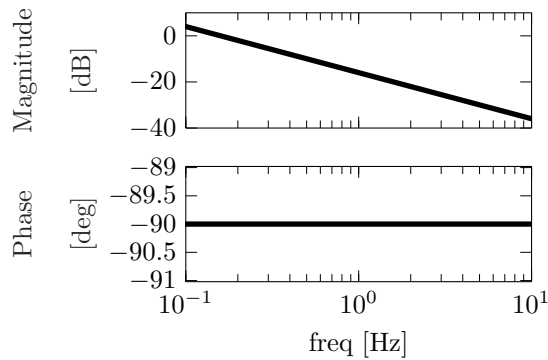


Figure 11: GP with constant, linear or Wiener covariance function: TF of the equivalent SDE system

4. Latent force modeling for Bayesian input-state estimation

The most common Kalman-based estimators, e.g., the AKF or the DKF, rely on a prior assumption regarding the dynamic model of the unknown input, which is constructed via a random-walk model. Although the random-walk is a widely adopted solution, it is sometimes not representative of the actual loading conditions a structure is subjected to. This results in the need of a user-dependent dedicated offline tuning procedure for the unknown input covariance, which strongly controls the force prediction accuracy. Indeed, for loads featuring complex dynamics, thus strongly deviating from the assumption of Brownian motion to which the random-walk belongs, the prediction accuracy may not reach satisfactory values. For this reason, this chapter proposes a prior transition equation for the unknown input shaped by a LFM derived from regression via GPs using training data.

4.1. Latent Force Models

A more flexible and comprehensive alternative to the conventional random-walk for establishing a prior model for the unknown input in a Kalman filtering setting consists in employing LFMs [42, 43], i.e., hybrid schemes that incorporate data-driven paradigms in a relatively simple mechanistic model. The key idea behind LFMs construction

is to make use of a mechanistic model of the system which is augmented via data-driven techniques in order to provide enough flexibility to allow for the resulting model to fit the actual system even when mechanistic assumptions are not precisely met. According to this approach, any model such as the one in Eq. 5, in which the system is forced by latent functions can be referred as LFM if the components of the forcing vector \mathbf{u} are modeled as zero-mean independent stochastic processes. Specifically, in a GPLFM framework, the j th component f^j of the forcing vector \mathbf{u} of the system in Eq. 5 is modeled as a zero-mean time-domain one-dimensional GP.

The approach proposed in [42, 43] stems from the assumption that the structural system state vector \mathbf{x} can be modeled as a multi-dimensional GP:

$$\mathbf{x}(t) \sim \mathcal{GP}(\mathbf{0}, \mathbf{K}_{\mathbf{xx}}(t, t')). \quad (54)$$

In absence of the independence assumption of the forcing terms, correlated terms would be admitted within the forcing vector, which would thus need to be modeled by correlated GPs, i.e., with non-zero off-diagonal terms in the covariance matrix. GP regression for full covariance matrices is addressed in literature via use of instantaneous mixing [65–67] or convolution [68–70] of a series of independent processes to construct correlated processes. These approaches require more advanced calculations and, consequently, additional computational effort. The independent forcing terms hypothesis is thus adopted in this work to simplify the construction of LFMs. This assumption does not introduce a too strict simplification within the context of Kalman-based input-state estimation algorithms, where prior information regarding the location and the direction of the unknown forcing terms is assumed to be available. Despite this simplification, the resulting LFM turns into a GP regression problem that still requires complex numerical integration for computing the covariance matrices, which may not always have a closed-form. A workaround to this problem consists in adopting the temporal state-space GP formulation to model the latent forcing terms, which are then used to augment the system mechanistic model resulting in a practical joint state-space form.

4.2. Latent Force Models for joint input-state estimation

The GPLFM approach has been originally adopted for input-state estimation in a Kalman filtering framework in [44] and further exploited in [46] for offline input-state-parameter estimation. An in-situ validation of the method has been provided in [45] and an extension to identification of mechanical systems with discontinuous nonlinearity has been proposed in [47] via the use of switching GPs. The basic principle consists in adopting a GP state-space representation derived to model the (unknown) latent forces acting on the system under the assumption of conventional covariance functions, i.e., squared exponential, exponential or Matérn type. The corresponding state-space model is then used in combination with the system state-space (mechanistic) model by augmenting the state vector \mathbf{x} with the input state vector \mathbf{z} defined in Eq. 24, yielding the final augmented model:

$$\begin{bmatrix} \dot{\mathbf{x}}(t) \\ \dot{\mathbf{z}}^{(1)}(t) \\ \dot{\mathbf{z}}^{(2)}(t) \\ \vdots \\ \dot{\mathbf{z}}^{(n_i)}(t) \end{bmatrix} = \begin{bmatrix} \mathbf{A} & \mathbf{b}_1 \mathbf{H}^{(1)} & \mathbf{b}_2 \mathbf{H}^{(2)} & \dots & \mathbf{b}_{n_i} \mathbf{H}^{(n_i)} \\ 0 & \mathbf{F}^{(1)} & 0 & \dots & 0 \\ 0 & 0 & \mathbf{F}^{(2)} & \dots & 0 \\ \vdots & \vdots & \vdots & \ddots & \vdots \\ 0 & 0 & 0 & \dots & \mathbf{F}^{(n_i)} \end{bmatrix} \begin{bmatrix} \mathbf{x}(t) \\ \mathbf{z}^{(1)}(t) \\ \mathbf{z}^{(2)}(t) \\ \vdots \\ \mathbf{z}^{(n_i)}(t) \end{bmatrix} + \begin{bmatrix} \mathbf{w}(t) \\ \tilde{\mathbf{w}}^{(1)}(t) \\ \tilde{\mathbf{w}}^{(2)}(t) \\ \vdots \\ \tilde{\mathbf{w}}^{(n_i)}(t) \end{bmatrix} \quad (55)$$

$$\mathbf{y}(t) = \begin{bmatrix} \mathbf{C} & \mathbf{g}_1 \mathbf{H}^{(1)} & \mathbf{g}_2 \mathbf{H}^{(2)} & \dots & \mathbf{g}_{n_i} \mathbf{H}^{(n_i)} \end{bmatrix} \begin{bmatrix} \mathbf{x}(t) \\ \mathbf{z}^{(1)}(t) \\ \mathbf{z}^{(2)}(t) \\ \vdots \\ \mathbf{z}^{(n_i)}(t) \end{bmatrix} + \mathbf{v}(t) \quad (56)$$

where $\mathbf{b}_1, \mathbf{b}_2, \dots, \mathbf{b}_{n_i}$ are the columns of the structural system \mathbf{B} matrix and $\mathbf{g}_1, \mathbf{g}_2, \dots, \mathbf{g}_{n_i}$ are the columns of the structural system \mathbf{G} matrix. $\tilde{\mathbf{w}}^{(j)}(t) \in \mathbb{R}^m$ is a vector-valued GP given by $\tilde{\mathbf{w}}^{(j)}(t) = \mathbf{L}^{(j)} \omega^{(j)}(t)$, with spectral density $\mathbf{Q}_c^{(j)} \in \mathbb{R}^{m \times m}$ expressed as $\mathbf{Q}_c^{(j)} = \mathbf{L}^{(j)} \mathbf{q}_c (\mathbf{L}^{(j)})^T$. In shorthand notation, the discrete-time version of the augmented state-space model shown in Eqs. 55 and 56, computed via an exponential time discretization scheme, can be expressed as follows:

$$\begin{cases} \mathbf{x}_k^a &= \mathbf{A}_d^a \mathbf{x}_{k-1}^a + \mathbf{w}_{k-1}^a \\ \mathbf{y}_k &= \mathbf{C}^a \mathbf{x}_k^a + \mathbf{v}_k \end{cases} \quad (57)$$

where $\mathbf{A}_d^a = e^{(\mathbf{A}^a \Delta t)}$ with $\mathbf{A}^a \in \mathbb{R}^{n_{aug} \times n_{aug}}$ being the state matrix in Eq. 55, while the output matrix $\mathbf{C}^a \in \mathbb{R}^{n_o \times n_{aug}}$, where $n_{aug} = 2n_r + m \times n_i$ if the LTI SDE in Eq. 22 is of the same order m for all the latent forces. \mathbf{w}_{k-1}^a is a discretized version of the augmented process noise vector $\mathbf{w}^a(t) \in \mathbb{R}^{n_{aug}}$, which is associated to the covariance matrix $\mathbf{Q}^a = \text{blkdiag} [\mathbf{Q}, \mathbf{Q}_c]$. In the last expression, \mathbf{Q} is the discretized version of the process noise covariance matrix associated with the state vector \mathbf{x} , while $\mathbf{Q}_c = \text{blkdiag} [\mathbf{Q}_c^1, \dots, \mathbf{Q}_c^{n_i}]$. As a result of the independence assumption made on the latent inputs, the error covariance matrix \mathbf{P}_k^a associated with the augmented state vector \mathbf{x}_k^a has a block diagonal form of the type:

$$\mathbf{P}_k^a = \text{blkdiag} [\mathbf{P}_k, \mathbf{P}_k^1, \dots, \mathbf{P}_k^{(j)}, \dots, \mathbf{P}_k^{n_i}] \quad (58)$$

where \mathbf{P}_k is the covariance matrix for the non-augmented state vector \mathbf{x}_k and $\mathbf{P}_k^{(j)}$ is the covariance matrix for the j -th latent force.

Joint recursive inference of states and inputs can be performed by employing the augmented system in Eq. 57 in a sequential scheme made up of a KF and a RTS smoother. Once the estimated augmented state vector $\hat{\mathbf{x}}_k^a$ has been obtained, it can be used for predicting the vector $\hat{\mathbf{y}}_k^e$ of the n_e unmeasured responses using the following formula:

$$\hat{\mathbf{y}}_k^e = \mathbf{C}_e^a \hat{\mathbf{x}}_k^a \quad (59)$$

where \mathbf{C}_e^a is the augmented output matrix computed at the DOFs where the response has to be estimated. It is worth noting that the GPLFM can be considered as a generalization of the augmented state-space model used in the well-known AKF, which normally features marginally stable transmission zeros when no displacement-level measurement is adopted. To the contrary, it has been found that the GPLFM always admits stable inversion since it has no marginally stable transmission zeros regardless of the adopted type of observations [44]. This property adds further flexibility to the use of the GPLFM for joint input-state estimation in real-life problem for any type of data set.

Although the validity of using GPLFMs as reported so far has been demonstrated in [44–47], the following considerations must be made.

- The GPLFM approach has been proposed in literature for specific and rather conventional classes of covariance functions, i.e., Matérn, squared exponential, exponential. In Section 3, the equivalent state-space representation of a GP featuring such covariance functions has been found to always have real and coincident roots with multiplicity dependent on the adopted Matérn smoothness parameter. The achieved state-space representation hence corresponds to a “critically damped” dynamic system whose response, i.e., the model imposed for the unknown input in the joint input-state estimation framework, has a time waveform dominated by the term $w(t)$ in Eq. 38 and modulated by an exponentially decaying trend. As a result, conventional covariance functions represent a generic and easy-to-derive modeling choice which, however, does not account for specific content that the input may feature, e.g. harmonics, biases, sudden changes. For this reason, additional covariance functions have been introduced in this work and the associated state-space models have been derived in Section 3. Among the proposed functions, periodic covariance functions allow for a dynamic model including undamped harmonics, thus representing the most suitable choice for regression of sinusoidal signals. However, real-life signals too often deviate from pure sinusoidals as they are noise-contaminated, affected by disturbances or rather obtained as compositions of signals of different nature, i.e., random multisines. To take these aspects into account, quasiperiodic covariance functions can be employed for regression. Additionally, linear and constant covariance functions can be adopted in combination with other covariance functions (to obtain, e.g. the biased quasiperiodic covariance function) to respectively model linear trends and biases in data. Finally, the Wiener covariance function can be exploited to construct an alternative and more flexible state-space model for the unknown input satisfying the random-walk assumption, thus finding its best application in regression of ambient noise signals. The hereby reported considerations will be extensively proved in Subsection 4.3, where the mentioned covariance functions will be employed for joint input-state estimation of a 3 DOFs system subject to inputs of different nature. Additionally, an experimental validation will be provided in Section 5.
- A sequence of a KF and a RTS smoother is proposed in literature as a solution for recursive regression via GPs. Including smoothing in the algorithm allows to obtain estimations at the current instant of time on the basis of past and future observations. The combination of a KF and a RTS smoother thus allows to exactly transfer GP regression from its batch to its recursive form. Nevertheless, this operation is in contrast with the more practical

need of deploying real-time estimators for operational and experimental data since it foresees a certain lag to be taken into account before acquiring estimations at a given instant of time. Additionally, Subsection 4.3 will show that including the smoothing step in the algorithm renders the resulting predictions more prone to accumulation errors. This work therefore proposes to exclude the RTS from the joint input-state estimation algorithm based on the GPLFM framework, thus running a forward KF only.

- The GP-based approach adopted in literature for joint input-state estimation foresees the use of the entire set of measurements used for the joint input-state estimation for selecting the covariance function hyperparameters. This implies that a substantially large set of observations needs to be acquired prior to the operational employment of the estimator. Additionally, the use of multiple signals for Bayesian model selection drastically increases the required computational time. To remedy these problems, the use of a single pre-recorded measurement will be proposed in this paper for both the simulated and the experimental case studies. It is worth noting that the most convenient choice for the pre-recorded signal corresponds to an acceleration signal at the unknown input location. Indeed, a collocated acceleration features a direct link to the unknown input via the feedthrough matrix. In absence of a collocated measurement, any other acceleration on the structure may be used to select the covariance function hyperparameters. Acceleration signals are instead not suitable in presence of biased inputs, e.g. a static load, as they do not provide static information. In this situations, a displacement-level signal should be adopted.

4.3. Joint input-state estimation of a 3 DOFs system via GPLFMs

This subsection makes use of the GPLFM approach for input-state estimation of the 3 DOFs system in Fig. 12, excited by a force applied at the 3rd mass. The system masses m_1 , m_2 and m_3 are assumed to be 100, 80 and 80 kg, respectively. The springs stiffness values have been selected as follows: $k_1 = 2 \times 10^5$, $k_2 = 1.5 \times 10^5$, $k_3 = 1.5 \times 10^5$ N/m. Damping has been defined assuming a proportional behavior such that $\mathbf{C} = 2 \times 10^{-2} \mathbf{M} + 3 \times 10^{-4} \mathbf{K}$. The system natural frequencies and damping ratios are provided in Tab. 1.

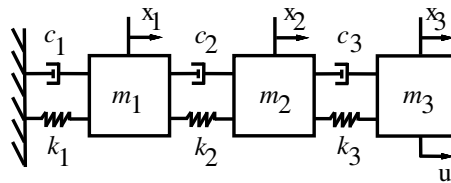


Figure 12: 3 DOFs system

Modes	1	2	3
Natural frequency [Hz]	3.26	8.52	12.16
Damping ratio [%]	0.36	0.82	1.16

Table 1: Natural frequencies and damping ratios of the 3 DOFs system

The proposed simulated example is hereby exploited to implement and prove the comments listed in the previous section. To explore the spectrum of covariance functions proposed in this work, the input-state prediction problem has been implemented for the 3 DOFs system under the assumption of several types of inputs acting on the 3rd mass, i.e., random, sine, random multisine, impulse, step. Every loading scenario has been addressed adopting the corresponding most suitable covariance function and the achieved input and response predictions have been compared with the results obtained via a conventional Matérn covariance function. Moreover, the hereby applied estimator is constructed using a KF only in order to guarantee real-time applicability. To validate this choice, predictions are compared to the ones achieved via sequential KF and RTS, for every loading case. The state process noise covariance matrix \mathbf{Q} and the measurement noise covariance matrix \mathbf{R} , necessary for the implementation of the adopted filtering and smoothing algorithms, have been set by trial and error and kept unchanged across all the loading scenarios for consistency. The trial and error process conducted to select these matrices has been based on differentiating the covariance order

of magnitude according to the associated quantity, e.g. displacements and velocities for \mathbf{Q} and displacements and accelerations for \mathbf{R} , to ensure a realistic quantification of the modeled errors. A single collocated “measurement”, i.e., a response simulated at the 3rd mass and contaminated by noise, is adopted as observation for input-state estimation. When the input has a step profile, the 3rd mass displacement is used as measurement to ensure that a static information is acquired [28]. Otherwise, a collocated acceleration measurement is preferred in order to guarantee a feedthrough term with the unknown input, and thus direct input-output coupling [28]. The same observed response time signal is also used in Eq. 11 for determining the covariance function hyperparameters prior to online estimation. For implementing the marginal likelihood optimization step, the initial hyperparameters values are chosen so as to avoid the method to incur in erroneous local minima.

Sine load

This paragraph reports on the input-state estimation results for the analyzed system excited by a sinusoidal input (1 Hz) applied at the 3rd mass. In this loading scenario, the use of a periodic covariance function (with period selected according to the sinusoidal excitation frequency) for constructing the GPLFM is strongly preferable to the conventional Matérn function since it allows to account for harmonic features within the adopted GP rather than relying on the “critically damped” Matérn model. Table 2 summarizes the selected initialization values of the parameters necessary for the algorithm. Figure 13 compares the actual input and 1st mass displacement against the predictions achieved using the GPLFM approach with filtering only. Both the predictions obtained via the proposed periodic covariance function and a Matérn covariance function ($\nu = 1.5$) are displayed in Fig. 13. A visual inspection of the results confirms that the periodic covariance function is more suitable for estimating signals featuring pure harmonic components. This is specifically applicable for simulated systems such as the one hereby analyzed, where external noise sources are limited and damping follows a precise model. To the contrary, when dealing with physical systems, selecting a periodic covariance function may correspond to a too strict assumption on the content of the analyzed signals. Indeed, noise can perturb the signal periodicity and damping may not follow the model used when defining the system state-space equations. To mitigate these effects, a quasiperiodic covariance function is to be preferred when treating real-life problems.

Initial state mean	Initial error cov. matrix	Initial hyperparameters periodic	Initial hyperparameters Matérn	Process noise cov. matrix (\mathbf{Q})	Measurement noise cov. matrix (\mathbf{R})
$\hat{\mathbf{x}}_{0 0}^a = \mathbf{0}$	$\hat{\mathbf{P}}_{0 0}^x = \mathbf{0}$	$\sigma^2 = 1 \times 10^{-1}$ $l = 5 \times 10^{-1}$ $t_{period} = 1$	$\sigma^2 = 5$ $l = 1 \times 10^{-2}$	$\mathbf{Q}_{displ} = 10^{-20} \times \mathbf{I}_{displ}$ $\mathbf{Q}_{vel} = 10^{-10} \times \mathbf{I}_{vel}$	$\mathbf{R}_{displ} = 10^{-15} \times \mathbf{I}_{displ}$ $\mathbf{R}_{acc} = 10^{-12} \times \mathbf{I}_{acc}$

Table 2: 3 DOFs system, sine load: estimators initialization values

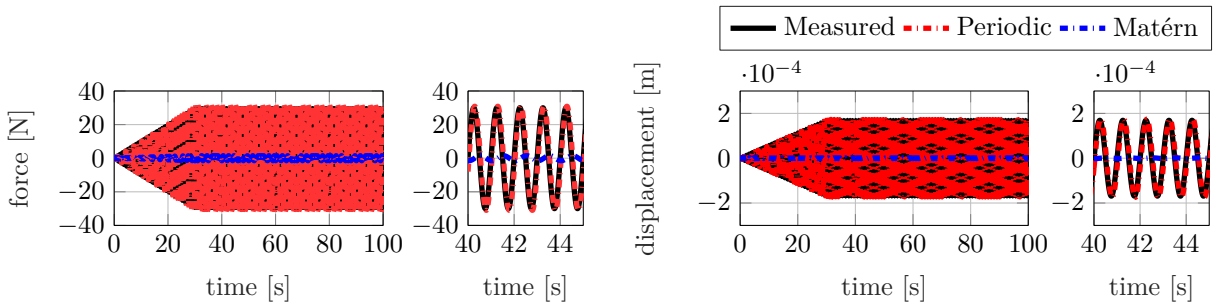


Figure 13: 3 DOFs system: time and detailed time histories of the sine input and the resulting 1st DOF displacement. “Measured” signals are shown by a solid black line, while those estimated (via filtering only) by making use of a periodic and a Matérn covariance function ($\nu = 1.5$) are respectively denoted via a dashed red and blue line.

A time-domain comparison between the results obtained via filtering only and the ones achieved via sequential KF and RTS smoother is offered in Fig. 14. By analyzing the displayed signals, it can be observed that combining filtering

and smoothing generates accumulation errors which result in low frequency components affecting the estimated time histories.

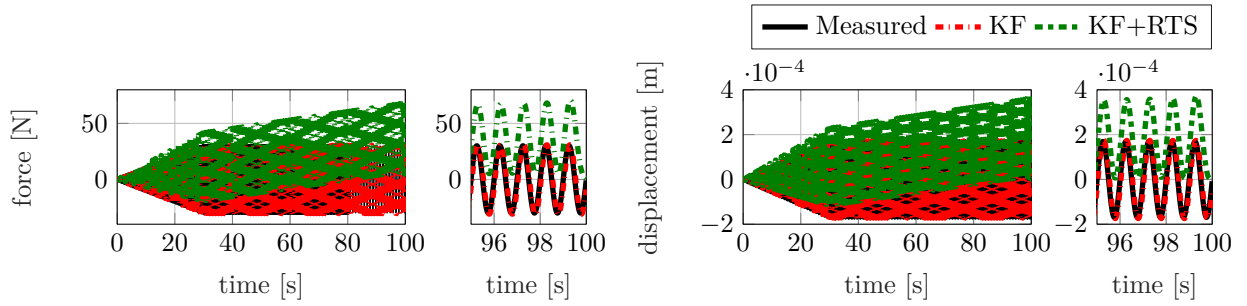


Figure 14: 3 DOFs system: time and detailed time histories of the sine input and the resulting 1st DOF displacement. “Measured” signals are shown by a solid black line, while those estimated by filtering only and a sequence of filtering and smoothing (periodic covariance function) are respectively denoted via a dashed red and green line.

A quantification of the estimation errors obtained by the analyzed estimators is reported in Tab. 3 for both the unknown force and the estimated responses by means of the Normalized Root Mean Square Error (NRMSE), i.e., the Root Mean Square Error (RMSE) between the estimated and the corresponding “measured” signal, normalized with respect to the “measured” signal Root Mean Square (RMS) value. Table 3 demonstrates that the employment of a periodic covariance function within a GPLFM solved with filtering only allows for the optimal performance of both input and response estimation in a sinusoidal loading scenario.

	NRMSE _{displ}			NRMSE _{vel}			NRMSE _{acc}			NRMSE mean resp.	NRMSE force
	DOF1	DOF2	DOF3	DOF1	DOF2	DOF3	DOF1	DOF2	DOF3		
Periodic (KF)	0.245	0.245	0.245	0.247	0.247	0.247	0.248	0.248	0.003	0.220	0.261
Matérn (KF)	1.001	1.001	1.000	0.999	1.001	0.994	0.963	1.042	0.982	0.998	1.001
Periodic (KF+RTS)	1.048	1.059	1.076	0.257	0.257	0.257	0.253	0.251	0.003	0.496	1.177

Table 3: 3 DOFs system, sine load: NRMSE values between “measured” and estimated signals (responses and force).

Random load

This paragraph reports on the input-state estimation results for the analyzed system excited by a pure random (white noise) input applied at the 3rd mass. In this loading scenario, the use of a Wiener covariance function for constructing the GPLFM is proposed as an alternative to the conventional Matérn function. As mentioned in Subsection 2.3, a GP with a Wiener covariance function is a random-walk model. Implementing a GPLFM approach for input-state prediction with a Wiener covariance function thus represents a non-conventional method for adopting a random-walk model for the unknown input. Unlike traditional Kalman-based estimators, where the random-walk assumption implies the need of a challenging tuning exercise, the GP-based formulation offers a flexible way for employing the random-walk model for input-state prediction. Indeed, in this framework the tuning effort is substituted with the preliminary training phase aimed at determining the hyperparameters. Following what stated in Section 3, it is evident that a Wiener covariance function represents the best choice for regression of purely random signals. Table 4 summarizes the selected initialization values of the necessary parameters for the algorithm.

Initial state mean	Initial error cov. matrix	Initial hyperparameters Wiener	Initial hyperparameters Matérn	Process noise cov. matrix (Q)	Measurement noise cov. matrix (R)
$\hat{\mathbf{x}}_{0 0}^a = \mathbf{0}$	$\hat{\mathbf{P}}_{0 0}^x = \mathbf{0}$	$\sigma^2 = 1 \times 10^{-4}$	$\sigma^2 = 5$ $l = 1 \times 10^{-2}$	$\mathbf{Q}_{\text{displ}} = 10^{-20} \times \mathbf{I}_{\text{displ}}$ $\mathbf{Q}_{\text{vel}} = 10^{-10} \times \mathbf{I}_{\text{vel}}$	$\mathbf{R}_{\text{displ}} = 10^{-15} \times \mathbf{I}_{\text{displ}}$ $\mathbf{R}_{\text{acc}} = 10^{-12} \times \mathbf{I}_{\text{acc}}$

Table 4: 3 DOFs system, random load: estimators initialization values

Figures 15 and 16 respectively compare the actual input and 1st mass displacement in time and frequency domains obtained via the proposed Wiener covariance function and the Matérn covariance function. The analysis of Figs. 15 and 16 proves that the use of the Matérn covariance function produces estimates featuring unrealistic frequency content, thus confirming that a Wiener covariance function allows to better capture the stochastic nature of the unknown input.

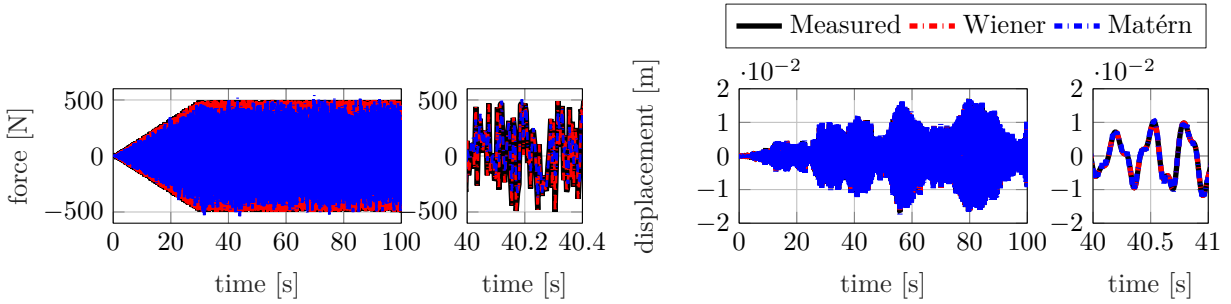


Figure 15: 3 DOFs system: time and detailed time histories of the random input and the resulting 1st DOF displacement. “Measured” signals are shown by a solid black line, while those estimated (via filtering only) by making use of a Wiener and a Matérn covariance function ($\nu = 1.5$) are respectively denoted via a dashed red and blue line.

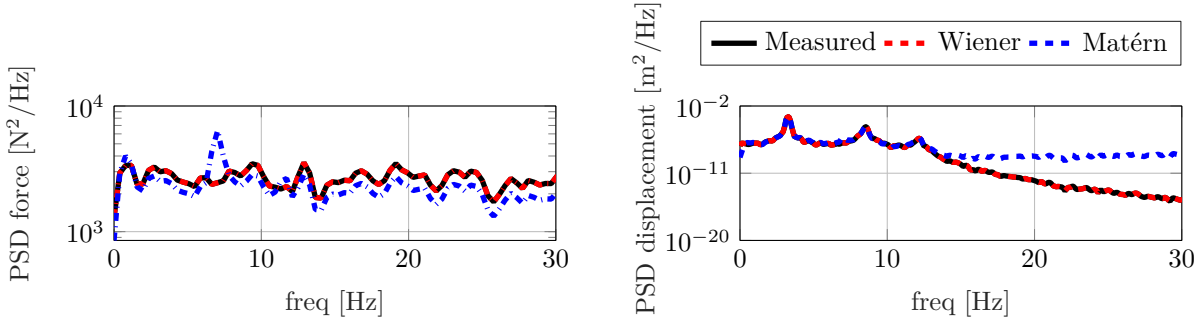


Figure 16: 3 DOFs system: Power Spectral Densities (PSDs) of the random input and the resulting 1st DOF displacement. “Measured” signals are shown by a solid black line, while those estimated (via filtering only) by making use of a Wiener and a Matérn covariance function ($\nu = 1.5$) are respectively denoted via a dashed red and blue line.

Figure 17 offers a time-domain comparison between the results obtained via filtering only and the ones achieved via sequential KF and RTS smoother. The input and response time histories estimated by combining filtering and smoothing show low frequency errors which are not generated when using Kalman filtering only.

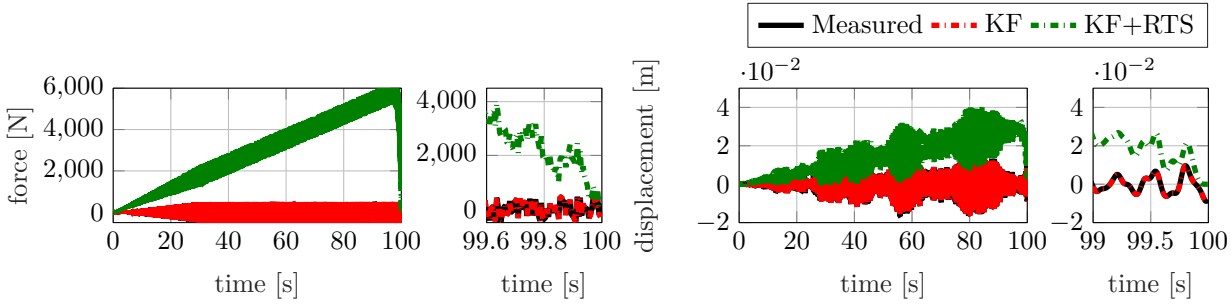


Figure 17: 3 DOFs system: time and detailed time histories of the random input and the resulting 1st DOF displacement. “Measured” signals are shown by a solid black line, while those estimated by filtering only and a sequence of filtering and smoothing (Wiener covariance function) are respectively denoted via a dashed red and green line.

Table 5 quantifies the estimation inaccuracy for the analyzed estimators by offering the NRMSE values computed between the estimated and the “measured” signals for both the unknown force and the predicted responses. Table 5 confirms that adopting a Wiener covariance function within a GPLFM solved with filtering only guarantees the highest performance for both input and response estimation in a random loading setting.

	NRMSE _{displ} × 10 ⁵			NRMSE _{vel} × 10 ⁵			NRMSE _{acc} × 10 ⁵			NRMSE × 10 ⁵ mean resp.	NRMSE force
	DOF1	DOF2	DOF3	DOF1	DOF2	DOF3	DOF1	DOF2	DOF3		
Wiener (KF)	0.078	0.091	0.111	0.003	0.002	0.001	0.005	0.005	0.010	0.034	0.014
Matérn (KF)	10178.163	11413.813	13798.689	5949.576	3661.975	1992.402	8319.623	7659.016	3143.413	734.630	0.459
Wiener (KF+RTS)	32660.282	38181.965	46559.658	635.706	445.016	318.899	829.560	742.271	158.739	13392.455	13.077

Table 5: 3 DOFs system, random load: NRMSE values between “measured” and estimated signals (responses and force).

Random multisine load

In this paragraph, the input-state predictions obtained for the 3 DOFs system subjected to a random multisine input at the 3rd mass are summarized. A random multisine signal is constructed as a superposition of sines with random phase within a selected frequency range (0-20 Hz). The use of a quasiperiodic covariance function is hereby proposed for representing this type of load and performing the hyperparameters training by regression of the 3rd mass acceleration. Indeed, adopting a quasiperiodic covariance function rather than a periodic one allows to simultaneously account for periodic and damping effects, which result from the random phase of the loading signal as well as the damped nature of the analyzed dynamical system. The initialization values for the algorithm under the different covariance assumptions are summarized in Tab. 6.

Initial state mean	Initial error cov. matrix	Initial hyperparameters quasiperiodic	Initial hyperparameters Matérn	Process noise cov. matrix (Q)	Measurement noise cov. matrix (R)
$\hat{\mathbf{x}}_{0 0}^a = \mathbf{0}$	$\hat{\mathbf{P}}_{0 0}^x = \mathbf{0}$	$\sigma^2 = 2 \times 10^{-2}$ $l = 3 \times 10^{-1}$ $t_{period} = 1$ $l_{matern} = 1.3$	$\sigma^2 = 5$ $l = 1 \times 10^{-2}$	$\mathbf{Q}_{displ} = 10^{-20} \times \mathbf{I}_{displ}$ $\mathbf{Q}_{vel} = 10^{-10} \times \mathbf{I}_{vel}$	$\mathbf{R}_{displ} = 10^{-15} \times \mathbf{I}_{displ}$ $\mathbf{R}_{acc} = 10^{-12} \times \mathbf{I}_{acc}$

Table 6: 3 DOFs system, random multisine load: estimators initialization values

Figures 18 and 19 compare the predictions obtained via the quasiperiodic and the Matérn covariance functions for the actual input and the 1st mass displacement in time and frequency domains respectively.

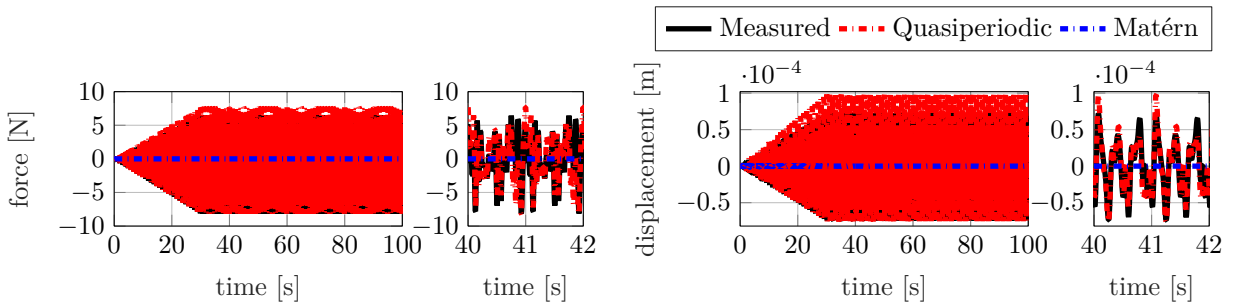


Figure 18: 3 DOFs system: time and detailed time histories of the multisine input and the resulting 1st DOF displacement. “Measured” signals are shown by a solid black line, while those estimated (via filtering only) by making use of a quasiperiodic and a Matérn covariance function ($\nu = 1.5$) are respectively denoted via a dashed red and blue line.

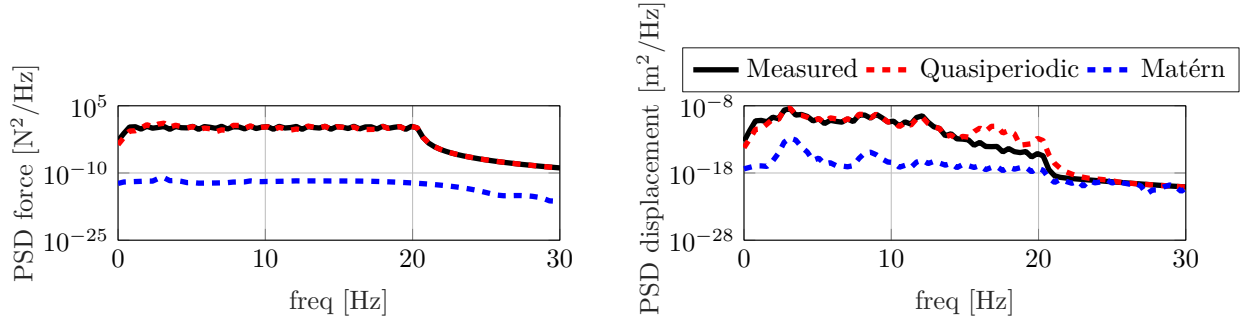


Figure 19: 3 DOFs system: PSDs of the multisine input and the resulting 1st DOF displacement. “Measured” signals are shown by a solid black line, while those estimated (via filtering only) by making use of a quasiperiodic and a Matérn covariance function ($\nu = 1.5$) are respectively denoted via a dashed red and blue line.

Figures 18 and 19 show that a quasiperiodic covariance function allows to better match the amplitude and the frequency content of the unknown input. The same conclusion can be drawn for the response estimate which, however, exhibits a slight mismatch between 15 and 20 Hz. This error can be explained by the use of only one acceleration observation, which reflects the input frequency content because of their direct feedthrough. Part of this content is then erroneously transferred to the response estimates of different type, i.e., displacement as the one in Figs. 18 and 19. This issue is normally solved in practical applications by including different types of responses within the observations set.

Figure 20 shows a time-domain comparison between the estimations obtained via filtering only and the ones achieved via sequential KF and RTS smoother. The input and response time histories estimated by combining filtering and smoothing exhibit a deviation error in the last two seconds of the analyzed time window. This effect only appears when smoothing is combined with filtering.

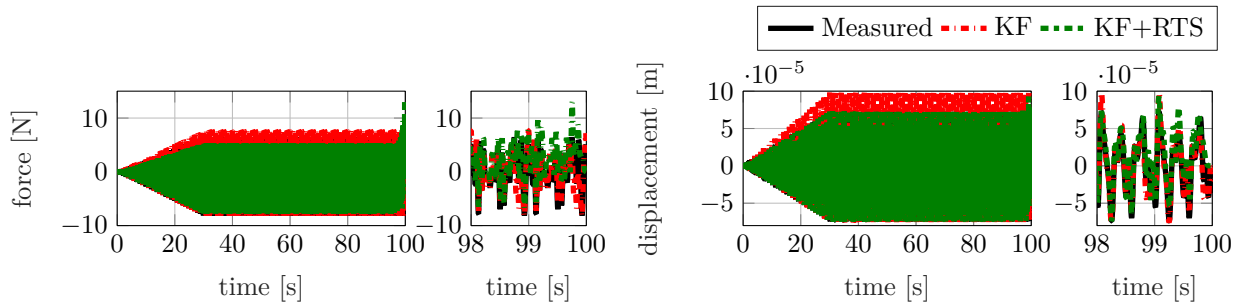


Figure 20: 3 DOFs system: time and detailed time histories of the multisine input and the resulting 1st DOF displacement. “Measured” signals are shown by a solid black line, while those estimated by filtering only and a sequence of filtering and smoothing (quasiperiodic covariance function) are respectively denoted via a dashed red and green line.

The overall highest prediction performance achieved under the assumption of a quasiperiodic covariance function (with filtering only) for a random multisine excitation is confirmed by Tab. 7, which reports on the NRMSE values computed between the estimated and the “measured” signals for both the unknown force and the estimated responses.

	NRMSE _{displ}			NRMSE _{vel}			NRMSE _{acc}			NRMSE mean resp.	NRMSE force
	DOF1	DOF2	DOF3	DOF1	DOF2	DOF3	DOF1	DOF2	DOF3		
Quasiperiodic (KF)	0.352	0.447	0.538	0.097	0.094	0.104	0.089	0.076	0.039	0.204	0.800
Matérn (KF)	1.000	1.000	1.000	1.000	1.000	1.000	1.000	1.000	1.000	1.000	1.000
Quasiperiodic (KF+RTS)	0.253	0.174	2.666	0.187	0.156	0.069	0.177	0.173	0.046	0.434	1.039

Table 7: 3 DOFs system, random multisine load: NRMSE values between “measured” and estimated signals (responses and force).

Impulse load

This paragraph treats the input-state predictions obtained for the 3 DOFs system when an impulse load is applied at the 3rd mass. A quasiperiodic covariance function is hereby compared with an exponential covariance function (Matérn with $\nu=0.5$) for regression of the 3rd mass acceleration and subsequent construction of the unknown input model. Indeed, a quasiperiodic covariance function is optimal for regression of damped dynamical systems free responses since these are expected to exhibit an oscillatory response with damped frequency content linked to the system modal properties. The exponential covariance function, i.e., a Matérn covariance function with $\nu = 0.5$, has been chosen as reference since this class of functions appear to be the most suitable for detecting large discontinuities in time due to the linked GPs being non-smooth, i.e., mean square non-differentiable. A summary of the initialization values selected for the algorithm parameters is reported in Tab. 8.

Initial state mean	Initial error cov. matrix	Initial hyperparameters quasiperiodic	Initial hyperparameters exponential	Process noise cov. matrix (\mathbf{Q})	Measurement noise cov. matrix (\mathbf{R})
$\hat{\mathbf{x}}_{0 0}^a = \mathbf{0}$	$\hat{\mathbf{P}}_{0 0}^x = \mathbf{0}$	$\sigma^2 = 6 \times 10^{-1}$ $l = 2.5 \times 10^{-1}$ $t_{period} = 0.3$ $l_{matern} = 1$	$\sigma^2 = 5$ $l = 1 \times 10^{-2}$	$\mathbf{Q}_{displ} = 10^{-20} \times \mathbf{I}_{displ}$ $\mathbf{Q}_{vel} = 10^{-10} \times \mathbf{I}_{vel}$	$\mathbf{R}_{displ} = 10^{-15} \times \mathbf{I}_{displ}$ $\mathbf{R}_{acc} = 10^{-12} \times \mathbf{I}_{acc}$

Table 8: 3 DOFs system, impulse load: estimators initialization values

Figure 21 (left) compares the actual input time history against the predictions achieved using the GPLFM approach with filtering only (both for a quasiperiodic and an exponential covariance function). Figure 21 (right) offers the time-domain estimation results for the 1st DOF displacement when a quasiperiodic or an exponential covariance function is adopted. Additionally, the corresponding PSDs are presented in Fig. 22.

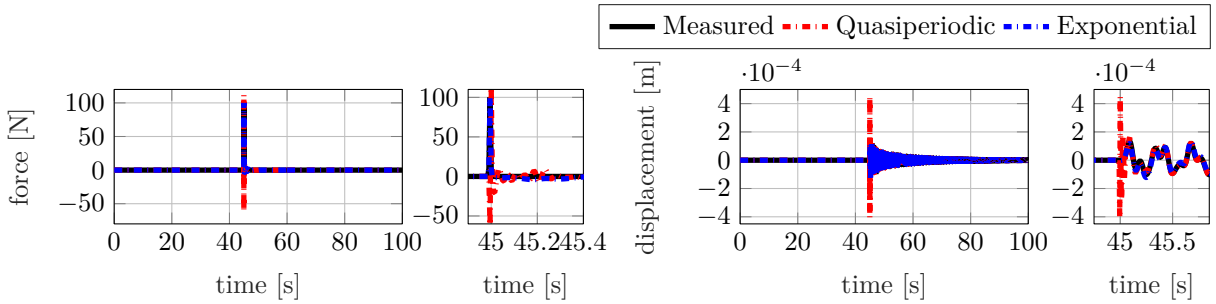


Figure 21: 3 DOFs system: time and detailed time histories of the impulse input and the resulting 1st DOF displacement. “Measured” signals are shown by a solid black line, while those estimated (via filtering only) by making use of a quasiperiodic and an exponential covariance function are respectively denoted via a dashed red and blue line.

From the analysis of Figs. 21 and 22 it can be concluded that the quasiperiodic covariance function generates larger estimation errors for both input and response estimations. This may be due to the quasiperiodic covariance function being centered on a specific frequency, e.g. the first natural frequency of the system, and only including its harmonics. This assumption excludes the possibility to include higher natural frequencies (2nd and 3rd for this application) in the GP representation and renders the hereby adopted quasiperiodic covariance function too strict for such application. A workaround for this limitation consists in constructing a covariance function as a product of quasiperiodic covariance functions centered at the 3 natural frequencies of the system.

Figure 23 shows a time-domain comparison between the estimations obtained via filtering only and the ones achieved via sequential KF and RTS smoother under the assumption of an exponential covariance function. The input and response time histories estimated by combining filtering and smoothing exhibit a deviation error in the last two seconds of the analyzed time window. These deviations are limited with respect to the ones experienced in the previously considered scenarios. This may be ascribed to the low signals amplitude at the end of the analyzed time frame for impulse response, which therefore generates lower accumulation errors.

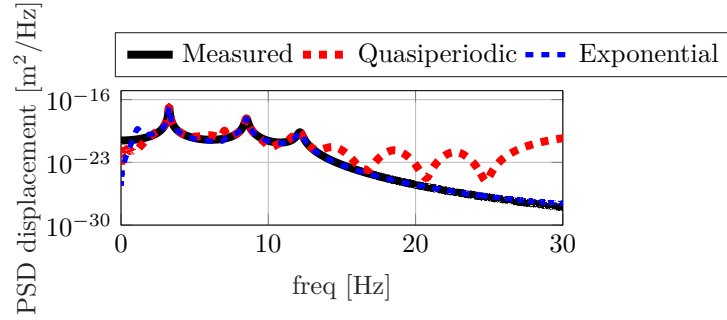


Figure 22: 3 DOFs system: PSDs of the 1st DOF displacement resulting from the impulse excitation. “Measured” signals are shown by a solid black line, while those estimated (via filtering only) by making use of a quasiperiodic and an exponential covariance function are respectively denoted via a dashed red and blue line.

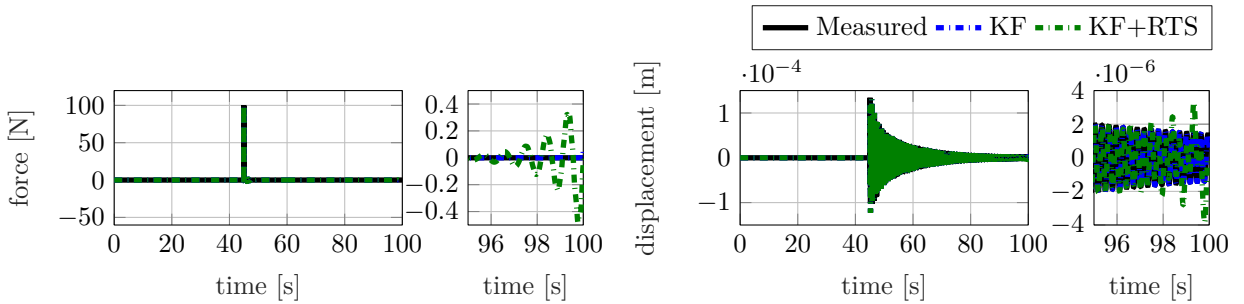


Figure 23: 3 DOFs system: time and detailed time histories of the impulse input and the resulting 1st DOF displacement. “Measured” signals are shown by a solid black line, while those estimated by filtering only and a sequence of filtering and smoothing (exponential covariance function) are respectively denoted via a dashed blue and green line.

A quantification of the estimation errors obtained by the analyzed estimators is reported in Tab. 9 by means of the NRMSE values computed between the estimated and the “measured” signals for both the unknown force and the estimated responses. Table 9 confirms that the use of a quasiperiodic covariance function centered at a specific frequency within a GPLFM generates large prediction inaccuracy for both the input and response estimations under an impulse excitation.

	NRMSE _{displ} × 10 ²			NRMSE _{vel} × 10 ²			NRMSE _{acc} × 10 ²			NRMSE × 10 ² mean resp.	NRMSE force
	DOF1	DOF2	DOF3	DOF1	DOF2	DOF3	DOF1	DOF2	DOF3		
Quasiperiodic (KF)	37.570	44.491	54.658	7.738	5.337	2.895	10.131	10.102	9.753	20.297	1.792
Exponential (KF)	8.541	9.800	11.660	3.756	3.688	3.836	3.851	3.776	0.023	5.437	0.332
Exponential (KF+RTS)	8.605	9.876	11.751	3.768	3.708	3.864	3.854	3.780	0.074	5.475	0.334

Table 9: 3 DOFs system, impulse load: NRMSE values between “measured” and estimated signals (responses and force).

Step load

In this paragraph, the input-state estimation results for the 3 DOFs system subjected to a step load are investigated. A quasiperiodic and an exponential covariance function have been selected for this problem following the same reasons standing for the impulse response. However, a step type of input features a static component which is normally difficult to identify via Bayesian estimators since these tools exploit a dynamical model of the system under study and a non-stationary model such as the random-walk for the unknown input. The GPLFM approach can remedy to this problem if: i) displacement-level sensors are included in the observations set; ii) a constant offset is included in the covariance function used for regression of a displacement-level response. A biased quasiperiodic covariance function, as explained

in Subsection 2.3, embeds a static component in the prior when performing regression. This allows to fit the bias present in a displacement response caused by a step input, thus guaranteeing its representation within the resulting unknown input model employed in the input-state estimation. The same approach has been used to build a biased exponential covariance function as a summation of a constant and an exponential (Matérn with $\nu = 0.5$) covariance function. The resulting covariance function has been adopted for estimation and results have been compared with the predictions obtained via the biased quasiperiodic covariance function. Table 10 presents an overview of the initialization values selected for the algorithm necessary parameters.

Initial state mean	Initial error cov. matrix	Initial hyperparameters biased quasiper.	Initial hyperparameters biased exp.	Process noise cov. matrix (\mathbf{Q})	Measurement noise cov. matrix (\mathbf{R})
$\hat{\mathbf{x}}_{0 0}^a = \mathbf{0}$	$\hat{\mathbf{P}}_{0 0}^x = \mathbf{0}$	$\sigma^2 = 2 \times 10^{-1}$ $\sigma_{constant}^2 = 2 \times 10^{-1}$ $l = 3 \times 10^{-1}$ $t_{period} = 0.3$ $l_{matern} = 1.3$	$\sigma^2 = 2 \times 10^{-1}$ $\sigma_{constant}^2 = 2 \times 10^{-1}$ $l = 3 \times 10^{-1}$	$\mathbf{Q}_{displ} = 10^{-20} \times \mathbf{I}_{displ}$ $\mathbf{Q}_{vel} = 10^{-10} \times \mathbf{I}_{vel}$	$\mathbf{R}_{displ} = 10^{-15} \times \mathbf{I}_{displ}$ $\mathbf{R}_{acc} = 10^{-12} \times \mathbf{I}_{acc}$

Table 10: 3 DOFs system, step load: estimators initialization values

Figure 24 (left) proposes a time-domain comparison between the actual input and the estimations achieved using the GPLFM approach with filtering only (both via the biased quasiperiodic covariance function and the biased exponential covariance function).

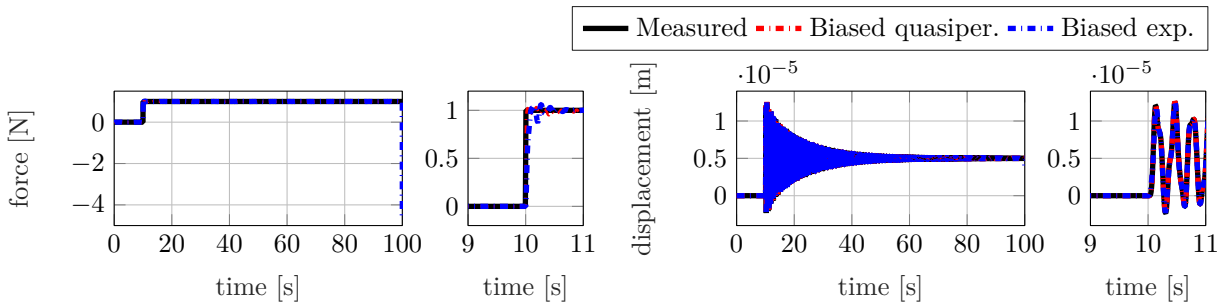


Figure 24: 3 DOFs system: time and detailed time histories of the step input and the resulting 1st DOF displacement. “Measured” signals are shown by a solid black line, while those estimated (via filtering only) by making use of a biased quasiperiodic and a biased exponential covariance function are respectively denoted via a dashed red and blue line.

The load time histories comparison shows that both the covariance functions allow to easily detect the step profile, but the biased exponential covariance function generates a large error at the last time instants of the analyzed time frame. Moreover, oscillations around the mean value are larger when adopting a biased exponential covariance function. Figure 24 (right) offers the actual 1st DOF displacement and the corresponding predictions achieved via the GPLFM approach in time domain. The presented comparison shows that a good response prediction can be obtained via both the analyzed covariance functions. However, by analyzing the PSDs comparison in Fig. 25, it can be concluded that the response estimate produced by the biased quasiperiodic covariance function better matches the “measured” response frequency content. These results are in contrast to the impulse response case, where the exponential covariance function provides more accurate estimations. This can be due to a different effect introduced by the constant covariance function when used in combination with a quasiperiodic or an exponential covariance function. While in both cases it allows to capture the bias, it may influence differently the hyperparameters values of the “dynamic” (quasiperiodic or exponential) covariance function selected during the training phase. As a generic conclusion, it can be stated that both the proposed covariance functions can be adopted for the analyzed loading scenario as the results deviation is limited.

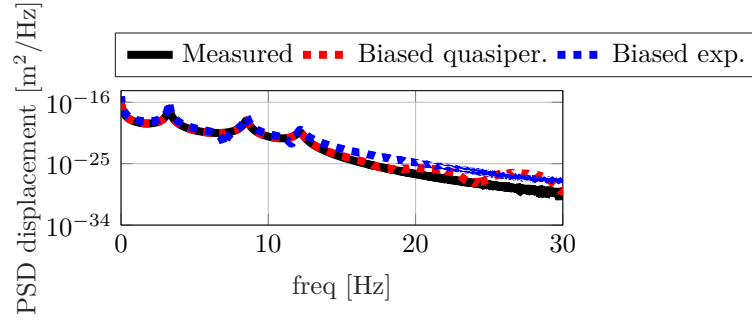


Figure 25: 3 DOFs system: PSDs of the 1st DOF displacement resulting from the step excitation. “Measured” signals are shown by a solid black line, while those estimated (via filtering only) by making use of a biased quasiperiodic and a biased exponential covariance function are respectively denoted via a dashed red and blue line.

Figure 26 offers a time-domain comparison between the results obtained via filtering only and the ones achieved via sequential KF and RTS smoother in the step loading scenario. The input and response time histories estimated by combining filtering and smoothing show large deviations at the end of the analyzed time window.

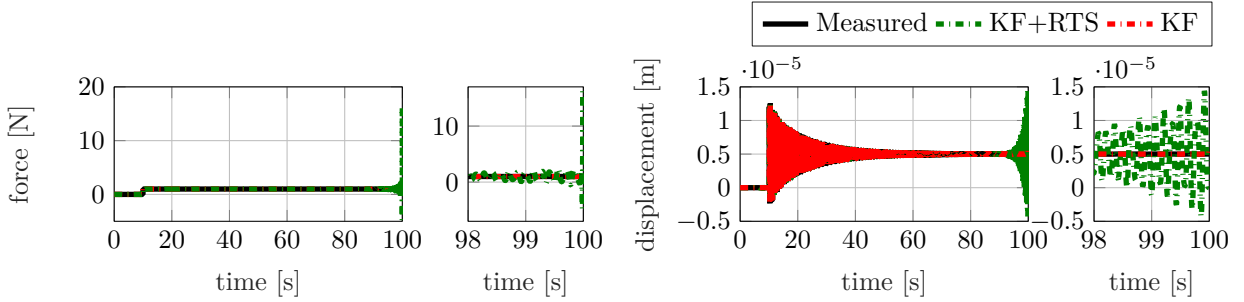


Figure 26: 3 DOFs system: time and detailed time histories of the step input and the resulting 1st DOF displacement. “Measured” signals are shown by a solid black line, while those estimated by filtering only and a sequence of filtering and smoothing (biased quasiperiodic covariance function) are respectively denoted via a dashed red and green line.

Table 11 quantifies the estimation inaccuracy for the analyzed estimators by offering the NRMSE values computed between the estimated and the “measured” signals for both the unknown force and the predicted responses. Table 11 proves that adopting a biased quasiperiodic covariance function within a GPLFM solved with filtering only allows for the optimal prediction performance for both input and responses under a step type of load.

	NRMSE _{displ}			NRMSE _{vel}			NRMSE _{acc}			NRMSE mean resp.	NRMSE force
	DOF1	DOF2	DOF3	DOF1	DOF2	DOF3	DOF1	DOF2	DOF3		
Biased quasiperiodic (KF)	0.016	0.017	0.005	0.173	0.251	0.180	0.287	0.428	0.513	0.208	0.055
Biased exponential (KF)	0.238	0.251	0.007	0.900	1.968	2.136	0.534	8.246	5.271	2.172	0.148
Biased quasiperiodic (KF+RTS)	0.040	0.023	0.009	0.328	0.205	0.212	0.765	0.611	0.488	0.298	0.066

Table 11: 3 DOFs system, step load: NRMSE values between “measured” and estimated signals (responses and force).

5. Case study: 3D-printed scaled titanium WT blade

The case study analyzed in this chapter concerns a 3D-printed scaled titanium WT blade [71]. The entire 3D-printed specimen, manufactured by 3D Systems (Leuven, Belgium), comprises the scaled blade and a flange which was designed to allow the blade clamping.

5.1. Measurement campaign

This section describes the setup adopted during the test campaign carried out at Siemens Industry Software (SISW) on the scaled blade, along with the series of tests performed with different types of excitation. Figure 27 (left) shows the setup adopted for the measurements on the scaled WT blade, during which the WT blade was clamped to a concrete block. The entire setup includes 3 types of sensors: 4 uniaxial strain gauges, 8 rosettes and 10 triaxial accelerometers. Figure 27 (right) shows the sensors locations. Strain sensors are arranged in sections along the blade on both the top and bottom surfaces, while accelerometers have been positioned only on the top surface.

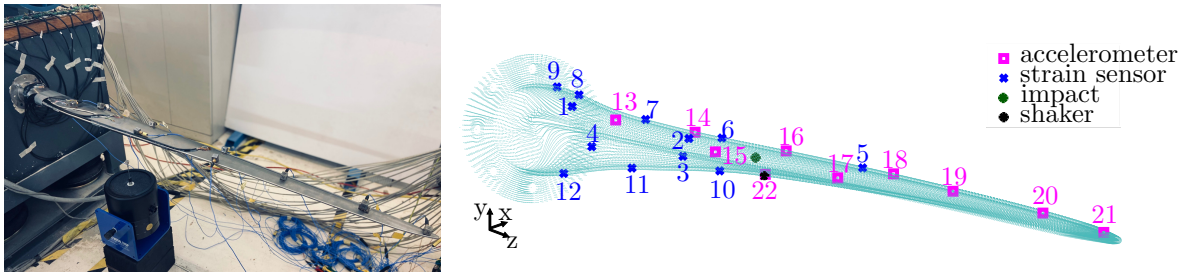


Figure 27: 3D-printed scaled titanium WT blade experimental setup (left) and sensing configuration (right): strain sensors (blue), accelerometers (magenta).

During the test campaign, a SimcenterTM SCADAS system and SimcenterTM Testlab software have been used for data acquisition. Three types of tests have been performed according to the adopted excitation method: impact testing using a modal hammer, shaker testing and the so-called pull and release tests. Figure 27 (right) shows the shaker and the impact locations. Data acquired during the impact test via the triaxial accelerometers has been used to determine the scaled WT blade modal properties in the frequency range of interest 0-450 Hz, which have been extracted using SimcenterTM PolyMAX. During shaker testing, constant frequency sine tests and continuous random tests up to 450 Hz were carried out. Finally, pull and release tests were performed by applying an initial static load via a mass (known weight equal to 1.5 kg) at the blade tip. During this test the blade is then released by cutting the plastic tie used to hang the mass. This leads to free vibrations of the blade, which are recorded via the installed sensors. It is worth noting that during shaker and pull and release tests, the main component of the recorded acceleration and strain are respectively oriented along the vertical (Y) and axial (Z) directions. Therefore, the remainder of the section will only consider accelerations along Y and strains along Z.

5.2. Numerical model

The scaled WT blade FE model shown in Fig. 28 (left), has been developed in SimcenterTM 3D starting from the Computer Aided Design (CAD) model used for 3D printing. The mesh is made up of around 65000 nodes and 33804 six-sided solid elements. The initial isotropic material (Ti6Al4V) properties have been defined according to the data sheet provided by the manufacturer. In order to reproduce the physical Boundary Conditions (BCs), the flange has been divided into four parts, each connected to a spring via a Rigid Body Element (RBE) connection. The free ends of the springs have been fixed. Additionally, concentrated masses have been added to the FE model at the accelerometers locations to account for their presence and increase the correlation with experimental data. Numerical modes in the frequency range 0-450 Hz have been computed using NXTM Nastran SOL 103. NXTM Nastran SOL 200 has been adopted in SimcenterTM 3D for updating the FE model using the experimental modal parameters as reference and a genetic algorithm for optimization. The following parameters have been set as design variables for the optimization process: springs stiffness, isotropic material Young's modulus, Poisson's ratio and density. Figure 28 (right) shows the final Modal Assurance Criterion (MAC) matrix between the reference experimental modes and the updated numerical modes.

A ROM of the scaled blade has been built following the procedure outlined in Subsection 2.1 taking into account the first six modes (frequency range of interest: 0-450 Hz) and one residual attachment mode related to the unknown force to be estimated via the chosen Bayesian estimators. For shaker tests, the residual attachment mode has been computed by applying a unitary force at the shaker location pointed out in Fig. 27 (right) along the positive Y direction. For pull and release tests, the unitary force for residual attachment mode computation has been applied at a tip node along the negative Y axis.

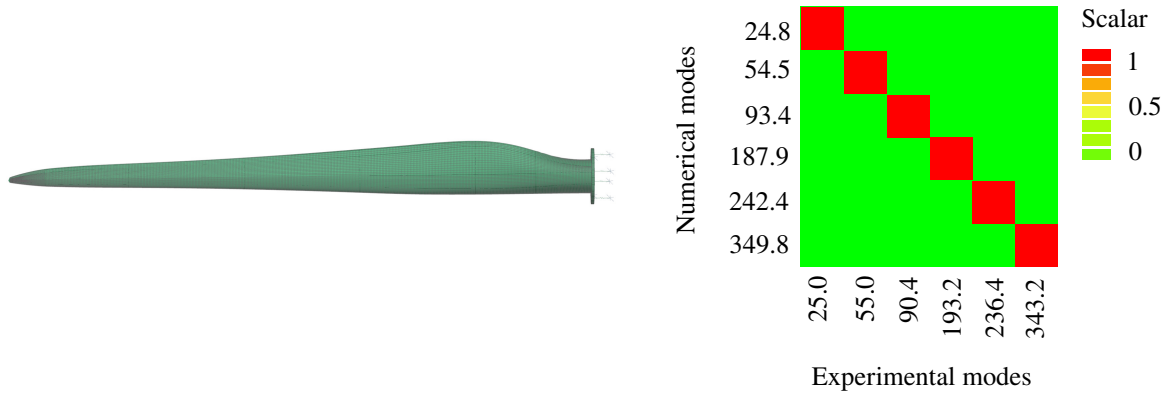


Figure 28: 3D-printed scaled titanium WT blade FE model (left). MAC between numerical and experimental mode shapes from hammer test (right).

5.3. Input-state estimation via GPLFMs

This section offers an experimental validation of the bespoke covariance function selection proposed in this work for input-state estimation via GPLFMs. By proposing a 3 DOFs example, Subsection 4.3 has proved that a proper covariance function selection plays an important role within the use of GPLFMs for estimating unknown loads and unmeasured structural responses in a Bayesian setting. In this section, three different loading conditions adopted during the 3D-printed scaled WT blade tests are treated: pull and release, random and sinusoidal load. For each loading condition, the most suitable covariance function is proposed in contrast to a conventional Matérn covariance function for construction of the LFM to be coupled with the scaled WT blade combined deterministic-stochastic state-space model. It is worth noting that i) the filtering-only version is hereby adopted for the GPLFM and ii) a single measurement is used for the training phase instead of the entire observations set. As mentioned in Subsection 4.2, the most convenient choice for the time signal to be used for training consists in adopting a pre-recorded measurement collocated with the unknown input [28]. Specifically, an acceleration signal is ideal for the random and sinusoidal load cases, while a displacement-level sensor, i.e., a strain signal, is preferred for the pull and release loading condition.

5.3.1. Pull and release test

This subsection proposes the use of a biased quasiperiodic covariance function for the GP adopted to construct the LFM for input-state estimation during the pull and release test performed on the 3D-printed scaled WT blade. The bespoke covariance function selection is validated by comparing the estimation results against the ones achieved by making use of a biased exponential (equivalent to a Matérn function with $\nu = 0.5$) covariance function. Specifically, sensor 1 has been hereby selected for training since no strain response collocated with the unknown load (applied at the tip) was available for this loading scenario. The hereby adopted estimators have been employed for input-state prediction using the mixed observations set (strain and acceleration) reported in Tab. 12. The measurements acquired at the remaining locations have been used to validate the estimations provided by the investigated methods. The chosen values for the necessary initial conditions, the states process noise covariance and the measurement noise covariance matrices are also shown in Tab. 12. Additionally, the analyzed GP covariance functions initial hyperparameters are presented in Tab. 12.

Figure 29 offers the predicted input signals provided by the GP-based approach when the two investigated covariance functions are adopted. Predictions are compared against the “measured” force, i.e., the step-type of input reconstructed on the basis of the known weight of the applied mass. Table 13 presents the Static Error (SE) and the Standard Deviation (SD) inaccuracy indicators for the two analyzed cases. The SE is formulated as the difference between the actual static input and the mean value of the estimated input profile. The SD, instead, quantifies the oscillations that affect the estimated time history after the blade release. Figure 29 highlights that the GPLFM with both the proposed covariance functions can easily detect the initial static load with limited inaccuracy. However, while the biased quasiperiodic covariance function allows for a correct detection of the release instant, the biased exponential covariance function produces a time history which does not follow the instantaneous release. Indeed, the estimated

Algorithm	Observations	Initial state mean	Initial error cov. matrix	Initial hyperparameters	Process noise cov. matrix (\mathbf{Q})	Measurement noise cov. matrix (\mathbf{R})
Biased exponential	1, 3, 8, 15, 17, 21	$\hat{\mathbf{x}}_{0 0}^a = \begin{bmatrix} \boldsymbol{\eta} \\ \mathbf{0} \end{bmatrix}$	$\hat{\mathbf{P}}_{0 0}^x = 10^{-10} \times \mathbf{I}$	$\sigma^2 = 1.5$ $\sigma_{constant}^2 = 1.1 \times 10^{-1}$ $l = 1 \times 10^{-1}$	$\mathbf{Q}_{displ} = 10^{-15} \times \mathbf{I}$ $\mathbf{Q}_{vel} = 10^{-7} \times \mathbf{I}$	$\mathbf{R}_{strain} = 10^{-14} \times \mathbf{I}$ $\mathbf{R}_{acc} = 10^{-7} \times \mathbf{I}$
Biased quasiperiodic	1, 3, 8, 15, 17, 21	$\hat{\mathbf{x}}_{0 0}^a = \begin{bmatrix} \boldsymbol{\eta} \\ \mathbf{0} \end{bmatrix}$	$\hat{\mathbf{P}}_{0 0}^x = 10^{-10} \times \mathbf{I}$	$\sigma^2 = 2 \times 10^{-1}$ $\sigma_{constant}^2 = 2 \times 10^{-1}$ $l = 3 \times 10^{-1}$ $t_{period} = 4 \times 10^{-2}$ $l_{matern} = 10^{-1}$	$\mathbf{Q}_{displ} = 10^{-15} \times \mathbf{I}$ $\mathbf{Q}_{vel} = 10^{-7} \times \mathbf{I}$	$\mathbf{R}_{strain} = 10^{-14} \times \mathbf{I}$ $\mathbf{R}_{acc} = 10^{-7} \times \mathbf{I}$

Table 12: 3D-printed scaled WT blade pull and release test: GPLFMs observations sets and initialization values for a biased exponential and a biased quasiperiodic covariance function

signal features a slow decay to zero which is reflected in both high SE and SD. It is therefore concluded that the use of a biased quasiperiodic covariance function to construct the GPLFM outperforms the biased exponential covariance function on the input estimation task during pull and release tests on the scaled WT blade.

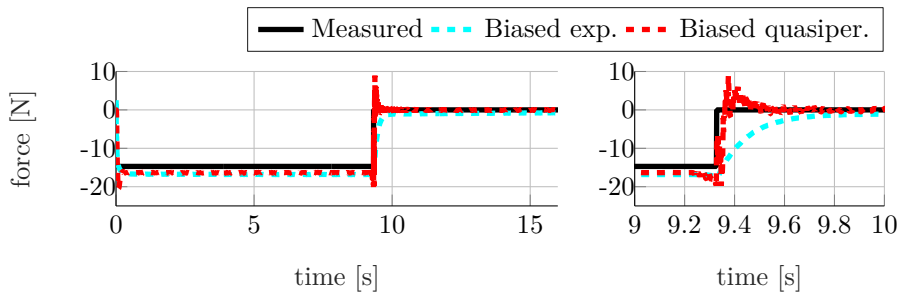


Figure 29: 3D-printed scaled WT blade pull and release test: input “measured” (black) and estimated (GPLFM with biased exponential cov. - cyan, GPLFM with biased quasiperiodic cov. - red) time histories (left) and detailed time histories (right)

	Biased exponential	Biased quasiperiodic
SE	11.23N	1.06N
SD	1.91N	0.20N

Table 13: 3D-printed scaled WT blade pull and release test: input prediction errors for the GPLFM with biased exponential and biased quasiperiodic covariance functions

Figures 30 and 31 show the time and frequency content of the responses estimated by the GPLFM algorithm for strain gauge 10 and accelerometer 14 when the analyzed covariance functions are used. In both cases, the estimated signals match their measured counterparts with relatively high accuracy.

A global analysis of the prediction results is offered in Tabs. 14 and 15 via the Time Response Assurance Criterion (TRAC) [50] values for the entire set of estimated responses (respectively strain and acceleration). The Frequency Response Assurance Criterion (FRAC) [50] values for the strain and acceleration responses are instead offered in Tabs. 16 and 17 respectively. The analysis of the TRAC and FRAC indicators shows that, while a similar result is achieved in terms of strain response estimation, the accuracy of acceleration response prediction is substantially higher when adopting a biased quasiperiodic covariance function. This is also demonstrated by the frequency content provided in Fig. 31, where a low frequency component erroneously affects the signal estimated by the biased exponential

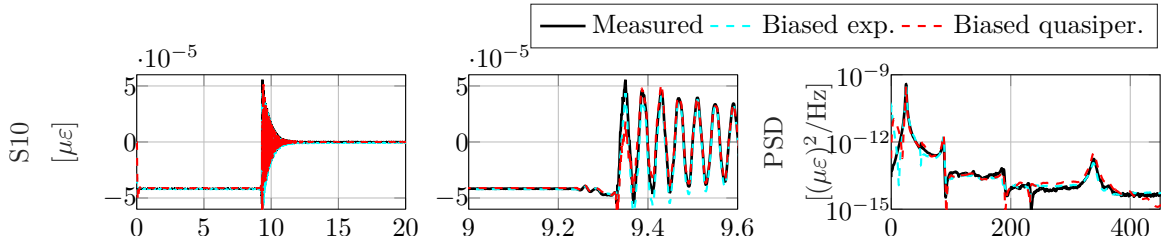


Figure 30: 3D-printed scaled WT blade pull and release test: measured (black) and estimated (GPLFM with biased exponential cov. - cyan, GPLFM with biased quasiperiodic cov. - red) strain at location 10

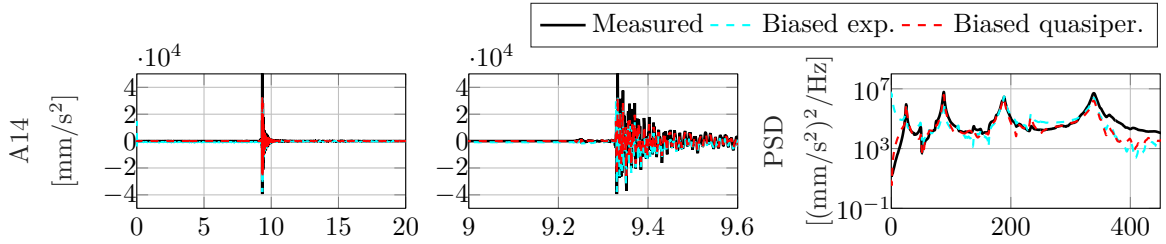


Figure 31: 3D-printed scaled WT blade pull and release test: measured (black) and estimated (GPLFM with biased exponential cov. - cyan, GPLFM with biased quasiperiodic cov. - red) acceleration at location 14

covariance function. To the contrary, the biased quasiperiodic covariance function produces a PSD which matches the measured signal in the entire reported frequency range (including low frequency).

Estimator	1	2	3	4	5	6	7	8	9	10	11	12
Biased exponential	<u>0.997</u>	0.997	<u>0.998</u>	0.998	0.996	0.998	0.998	<u>0.998</u>	0.995	0.997	0.998	0.998
Biased quasiperiodic	<u>0.994</u>	0.995	<u>0.995</u>	0.994	0.995	0.995	0.995	<u>0.993</u>	0.989	0.995	0.995	0.995

Table 14: 3D-printed scaled WT blade pull and release test: TRAC values between measured and estimated (GPLFM with biased exponential and biased quasiperiodic covariance functions) strain responses. Observations are underlined.

Estimator	13	14	15	16	17	18	19	20	21
Biased exponential	0.282	0.459	<u>0.997</u>	0.961	<u>1.000</u>	0.971	0.408	0.729	<u>1.000</u>
Biased quasiperiodic	0.762	0.866	<u>1.000</u>	0.961	<u>1.000</u>	0.973	0.904	0.931	<u>1.000</u>

Table 15: 3D-printed scaled WT blade pull and release test: TRAC values between measured and estimated (GPLFM with biased exponential and biased quasiperiodic covariance functions) acceleration responses. Observations are underlined.

Estimator	1	2	3	4	5	6	7	8	9	10	11	12
Biased exponential	<u>0.992</u>	0.988	<u>0.996</u>	0.999	0.919	0.993	0.998	<u>0.999</u>	0.999	0.990	0.997	0.998
Biased quasiperiodic	<u>0.982</u>	0.991	<u>0.994</u>	0.997	0.972	0.993	0.996	<u>0.997</u>	0.997	0.992	0.995	0.996

Table 16: 3D-printed scaled WT blade pull and release test: FRAC values between measured and estimated (GPLFM with biased exponential and biased quasiperiodic covariance functions) strain responses. Observations are underlined.

Estimator	13	14	15	16	17	18	19	20	21
Biased exponential	0.445	0.604	<u>1.000</u>	0.991	<u>1.000</u>	0.984	0.481	0.954	<u>1.000</u>
Biased quasiperiodic	0.837	0.864	<u>1.000</u>	0.992	<u>1.000</u>	0.981	0.994	0.985	<u>1.000</u>

Table 17: 3D-printed scaled WT blade pull and release test: FRAC values between measured and estimated (GPLFM with biased exponential and biased quasiperiodic covariance functions) acceleration responses. Observations are underlined.

5.3.2. Random test

This subsection proposes the use of a Wiener covariance function for the GP adopted within the LFM constructed for input-state estimation during random tests performed on the 3D-printed scaled WT blade. The bespoke covariance function selection is validated by comparing the estimation results against the ones achieved by making use of a conventional Matérn covariance function ($\nu = 1.5$) for the mixed observations set (strain and acceleration) reported in Tab. 18. The chosen values for the necessary initial conditions and the process and measurement noise covariance matrices are also summarized in Tab. 18. Additionally, the analyzed GP covariance functions initial hyperparameters are presented in Tab. 18. The hyperparameters have been tuned during the training phase by maximizing the log marginal likelihood of the acceleration collocated with the unknown input, i.e., at the shaker location indicated in Fig. 27 (right).

Estimator	Observations	Initial state mean	Initial error cov. matrix	Initial hyperparameters	Process noise cov. matrix (\mathbf{Q})	Measurement noise cov. matrix (\mathbf{R})
Matérn	1, 3, 8, 12, 15, 18, 21, 22	$\hat{\mathbf{x}}_{0 0}^a = \mathbf{0}$	$\hat{\mathbf{P}}_{0 0}^a = 10^{-10} \times \mathbf{I}$	$\sigma^2 = 3 \times 10^3$ $l = 2 \times 10^{-4}$	$\mathbf{Q}_{displ} = 10^{-20} \times \mathbf{I}$ $\mathbf{Q}_{vel} = 10^{-10} \times \mathbf{I}$	$\mathbf{R}_{strain} = 10^{-14} \times \mathbf{I}$ $\mathbf{R}_{acc} = 10^{-7} \times \mathbf{I}$
Wiener	1, 3, 8, 12, 15, 18, 21, 22	$\hat{\mathbf{x}}_{0 0}^x = \mathbf{0}$	$\hat{\mathbf{P}}_{0 0}^x = 10^{-10} \times \mathbf{I}$	$\sigma^2 = 3 \times 10^3$	$\mathbf{Q}_{displ} = 10^{-20} \times \mathbf{I}$ $\mathbf{Q}_{vel} = 10^{-10}$	$\mathbf{R}_{strain} = 10^{-14} \times \mathbf{I}$ $\mathbf{R}_{acc} = 10^{-7} \times \mathbf{I}$

Table 18: 3D-printed scaled WT blade random test: GPLFMs observations sets and initialization values for a Matérn ($\nu=1.5$) and a Wiener covariance function

Figure 32 offers a comparison in both time and frequency domains between the actual force, recorded by a force cell during the test, and the input predictions obtained by adopting the GPLFM in combination with a Wiener and a Matérn covariance function ($\nu = 1.5$). A quantification of the input estimations accuracy in time and frequency domains is respectively reported in Tabs. 20 and 22 (last column) by means of the TRAC and FRAC estimators. From the results reported in Tabs. 20 and 22, it can be concluded that a Wiener covariance function allows for higher input estimation accuracy. Figure 32 indeed highlights that the Matérn covariance function generates a distorted frequency content between 0 and 100 Hz.

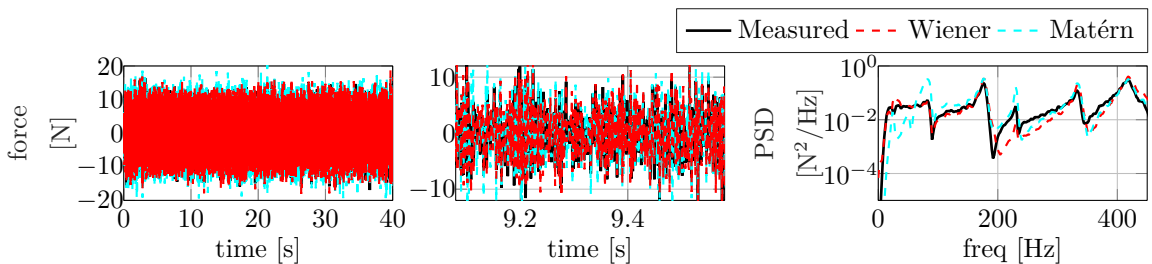


Figure 32: 3D-printed scaled WT blade random test: input measured (black) and estimated (GPLFM with Matérn cov. - cyan, GPLFM with Wiener cov. - red) force signals

Figures 33 and 34 present the comparison between measured and estimated signals respectively for a strain and an accelerometer that are not included in the observations set. These results demonstrate that a good prediction accuracy can be achieved by the GPLFM for both strain and acceleration predictions when each of the two analyzed covariance functions is adopted. However, the Matérn covariance function seems to produce a mismatch between 0 and 90 Hz in both the strain and the acceleration response. An overall information regarding the response estimation precision is reported in Tabs. 19-22 by means of the TRAC and FRAC indicators. The presented indicators show higher values (especially for strains) when the Wiener covariance function is adopted, confirming the conclusion drawn from Figs. 33 and 34.

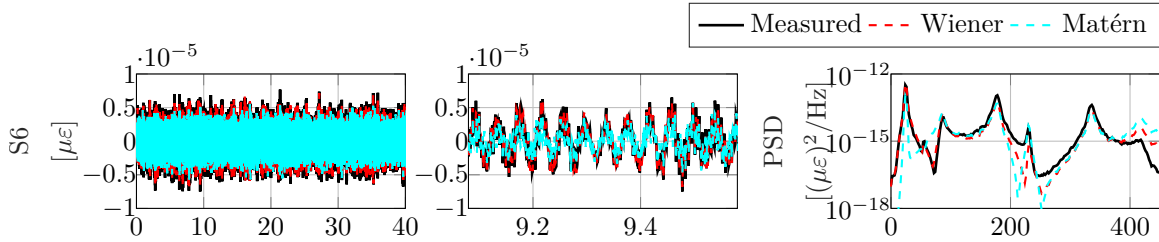


Figure 33: 3D-printed scaled WT blade random test: measured (black) and estimated (GPLFM with Matérn cov. - cyan, GPLFM with Wiener cov. - red) strain at location 6

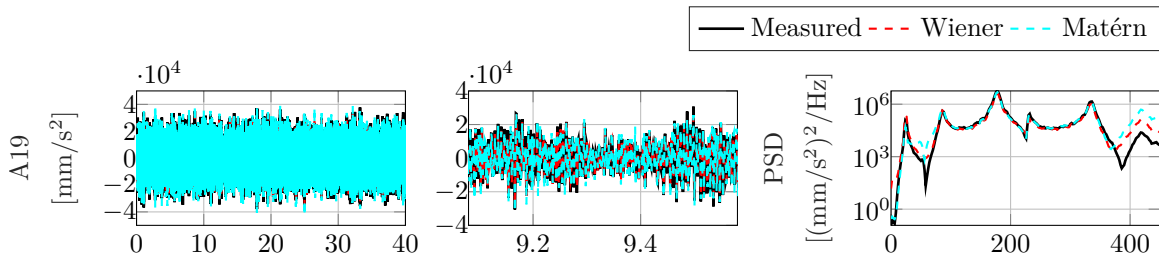


Figure 34: 3D-printed scaled WT blade random test: measured (black) and estimated (GPLFM with Matérn cov. - cyan, GPLFM with Wiener cov. - red) acceleration at location 19

Estimator	1	2	3	4	5	6	7	8	9	10	11	12
Matérn	<u>0.595</u>	0.584	<u>0.513</u>	0.510	0.743	0.601	0.652	<u>0.654</u>	0.693	0.581	0.630	<u>0.607</u>
Wiener	<u>0.938</u>	0.848	<u>0.825</u>	0.889	0.828	0.903	0.889	<u>0.959</u>	0.951	0.853	0.943	<u>0.942</u>

Table 19: 3D-printed scaled WT blade random test: TRAC values between measured and estimated (GPLFM with Matérn and Wiener covariance functions) strain responses. Observations are underlined.

Estimator	13	14	15	16	17	18	19	20	21	22	force
Matérn	0.914	0.494	<u>1.000</u>	0.305	0.095	<u>1.000</u>	0.882	0.558	<u>1.000</u>	<u>0.977</u>	0.642
Wiener	0.913	0.532	<u>0.988</u>	0.329	0.109	<u>0.964</u>	0.960	0.628	<u>0.989</u>	<u>0.999</u>	0.863

Table 20: 3D-printed scaled WT blade random test: TRAC values between measured and estimated (GPLFM with Matérn and Wiener covariance functions) force and acceleration responses. Observations are underlined.

Estimator	1	2	3	4	5	6	7	8	9	10	11	12
Matérn	<u>0.730</u>	0.673	<u>0.937</u>	0.943	0.907	0.912	0.855	<u>0.851</u>	0.899	0.794	0.756	<u>0.878</u>
Wiener	<u>0.961</u>	0.890	<u>0.931</u>	0.974	0.786	0.936	0.9867	<u>0.968</u>	0.977	0.920	0.993	<u>0.997</u>

Table 21: 3D-printed scaled WT blade random test: FRAC values between measured and estimated (GPLFM with Matérn and Wiener covariance functions) strain responses. Observations are underlined.

Estimator	13	14	15	16	17	18	19	20	21	22	force
Matérn	0.981	0.239	<u>1.000</u>	0.107	0.702	<u>1.000</u>	0.979	0.842	<u>1.000</u>	<u>0.943</u>	0.781
Wiener	0.969	0.280	<u>0.973</u>	0.109	0.594	<u>0.966</u>	0.997	0.831	<u>1.000</u>	<u>0.997</u>	0.937

Table 22: 3D-printed scaled WT blade random test: FRAC values between measured and estimated (GPLFM with Matérn and Wiener covariance functions) force and acceleration responses. Observations are underlined.

5.3.3. Sine test

The use of a quasiperiodic covariance function for constructing a GPLFM is hereby explored for input-state estimation during sinusoidal tests ($f_{sine} = 86Hz$) performed on the 3D-printed scaled WT blade. As anticipated in Subsection 4.2, experimentally recorded data are often affected by external sources of disturbance. For this reason, even when a sinusoidal signal is selected to drive the shaker, the actual load acting on the structure and recorded by the load cell may deviate from the pure sine assumption. To take this effect into account when constructing the GPLFM, a quasiperiodic covariance function is preferred to a periodic covariance function. The bespoke covariance function selection is hereby adopted for prediction during sine tests using the mixed observations set (strain and acceleration) reported in Tab. 23. The estimation results are compared against the ones achieved by making use of the same measurements set in combination with a conventional Matérn covariance function ($\nu = 1.5$). The chosen values for the necessary initial conditions and the process and measurement noise covariance matrices are also shown, along with the GP covariance functions initial hyperparameters. The initial period of the quasiperiodic covariance function has been set such that $t_{period} = 1/f_{sine}$. The hyperparameters have been selected by maximizing the log marginal likelihood of the acceleration collocated with the unknown input, i.e., at the shaker location indicated in Fig. 27 (right).

Estimator	Observations	Initial state mean	Initial error cov. matrix	Initial hyperparameters	Process noise cov. matrix (\mathbf{Q})	Measurement noise cov. matrix (\mathbf{R})
Matérn	1, 3, 8, 12, 15, 18, 21, 22	$\hat{\mathbf{x}}_{0 0}^a = \mathbf{0}$	$\hat{\mathbf{\Gamma}}_{0 0}^a = 10^{-10} \times \mathbf{I}$	$\sigma^2 = 3 \times 10^3$ $l = 2 \times 10^{-4}$	$\mathbf{Q}_{displ} = 10^{-20} \times \mathbf{I}$ $\mathbf{Q}_{vel} = 10^{-10} \times \mathbf{I}$	$\mathbf{R}_{strain} = 10^{-14} \times \mathbf{I}$ $\mathbf{R}_{acc} = 10^{-7} \times \mathbf{I}$
Quasiperiodic	1, 3, 8, 12, 15, 18, 21, 22	$\hat{\mathbf{x}}_{0 0}^a = \mathbf{0}$	$\hat{\mathbf{\Gamma}}_{0 0}^x = 10^{-10} \times \mathbf{I}$	$\sigma^2 = 5 \times 10^{-1}$ $l = 5 \times 10^{-1}$ $t_{period} = 1.2 \times 10^{-2}$ $l_{matern} = 8 \times 10^{-1}$	$\mathbf{Q}_{displ} = 10^{-20} \times \mathbf{I}$ $\mathbf{Q}_{vel} = 10^{-10}$	$\mathbf{R}_{strain} = 10^{-14} \times \mathbf{I}$ $\mathbf{R}_{acc} = 10^{-7} \times \mathbf{I}$

Table 23: 3D-printed scaled WT blade sine test: GPLFMs observations sets and initialization values for a Matérn ($\nu=1.5$) and a quasiperiodic covariance function

Figure 35 offers a time domain comparison between the actual force and the input predictions obtained via the GPLFM with a quasiperiodic and a Matérn covariance function. During the tests, the force applied by the shaker has been recorded by a force cell placed between the shaker and the structure. A quantification of the input estimations accuracy is reported in Tab. 25 (last column) by means of the TRAC estimator. From the results reported in Fig. 35, it can be concluded that while the GPLFM with a Matérn covariance function overestimates the load amplitude, a more accurate estimation is obtained via the GPLFM with a quasiperiodic covariance function. This result is confirmed by the TRAC values offered in Tab. 25.

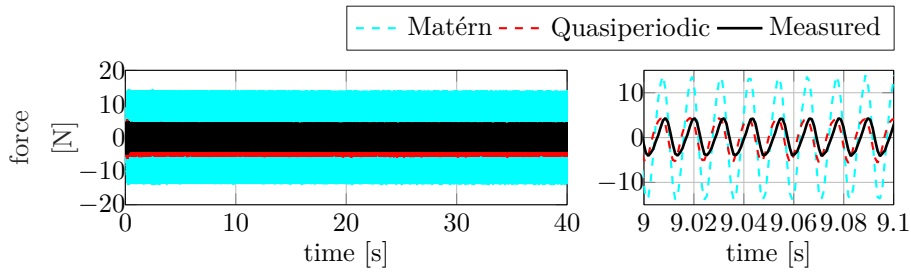


Figure 35: 3D-printed scaled WT blade sine test: input measured (black) and estimated (GPLFM with Matérn cov. - cyan, GPLFM with quasiperiodic cov. - red) force signals

Figures 36 and 37 present the comparison between measured and estimated signals respectively for a strain and an accelerometer that are not included in the observations set. These results demonstrate that a good and comparable prediction accuracy can be achieved by the GPLFM with a quasiperiodic or a Matérn covariance function for both strain and acceleration predictions. An overall information regarding the response estimation precision is reported in Tabs. 24 and 25 by means of the TRAC values. The presented indicators show comparable values for both strain and acceleration responses when the GPLFM is adopted with one of the two analyzed covariance functions.

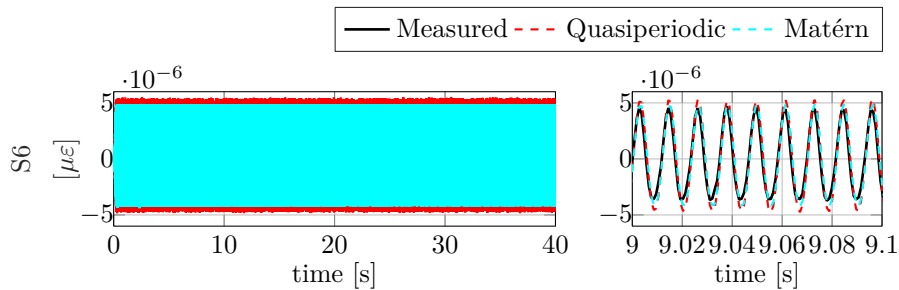


Figure 36: 3D-printed scaled WT blade sine test: measured (black) and estimated (GPLFM with Matérn cov. - cyan, GPLFM with quasiperiodic cov. - red) strain at location 6

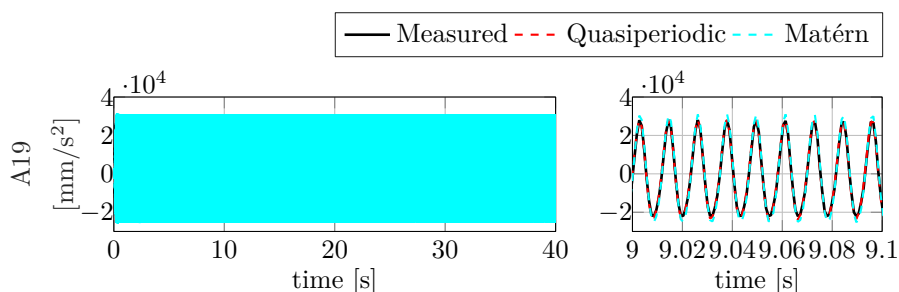


Figure 37: 3D-printed scaled WT blade sine test: measured (black) and estimated (GPLFM with Matérn cov. - cyan, GPLFM with quasiperiodic cov. - red) acceleration at location 19

The content offered in this section provides an experimental validation of the concepts elaborated in Subsection 4.2 and proved numerically in Subsection 4.3. The bespoke covariance function selection for GPLFMs construction in the framework of joint input-state estimation is hereby evaluated during tests on the 3D-printed scaled blade under different loading conditions. The produced results prove that a proper a priori selection of the covariance function allows to considerably enhance the achievable load estimation accuracy.

Estimator	1	2	3	4	5	6	7	8	9	10	11	12
Matérn	<u>0.994</u>	0.988	<u>0.221</u>	0.999	1.000	0.946	0.997	<u>0.994</u>	0.992	0.987	0.995	<u>0.992</u>
Quasiperiodic	<u>0.981</u>	0.985	<u>0.685</u>	0.889	0.997	0.968	0.988	<u>0.994</u>	0.985	0.996	1.000	<u>0.999</u>

Table 24: 3D-printed scaled WT blade sine test: TRAC values between measured and estimated (GPLFM with Matérn and quasiperiodic covariance functions) strain responses. Observations are underlined.

Estimator	13	14	15	16	17	18	19	20	21	22	force
Matérn	0.986	0.976	<u>1.000</u>	0.923	0.998	<u>1.000</u>	0.997	0.998	<u>1.000</u>	<u>1.000</u>	0.767
Quasiperiodic	0.989	0.986	<u>1.000</u>	0.947	0.998	<u>0.999</u>	0.995	0.999	<u>1.000</u>	<u>1.000</u>	0.812

Table 25: 3D-printed scaled WT blade sine test: TRAC values between measured and estimated (GPLFM with Matérn and quasiperiodic covariance functions) force and acceleration responses. Observations are underlined.

6. Conclusions

This paper elaborates on the necessary unknown input modeling, referred to as latent force modeling, for construction of Bayesian input-state estimators. Specifically, the use of structured LFMs is hereby proposed as a more comprehensive and flexible alternative to the commonly adopted random-walk transition model. A structured LFM can be constructed by exploiting the SDE representation for GP regression, which exhibits different features according to the chosen GP kernel. This work offers the SDE formulation for non-conventional covariance functions in the structural dynamics context. The analysis has been conducted through an analogy with harmonic oscillators, which has highlighted the tendency of certain classes of kernels towards a better regression performance in specific loading conditions. In particular, periodic or quasiperiodic kernels can be used to model expected harmonic components respectively in absence or in presence of damping. Constant covariance functions can be exploited to model biases in data, which may occur under static loading conditions. Finally, the Wiener covariance function provides a GPLFM formulation equivalent to the random-walk model, thus representing an optimal solution for estimation of randomic signals. The selection of bespoke GP covariance functions for estimation of standard excitation signals in vibration measurements is thus proposed in this work. The study is validated via a simulated 3 DOFs example and an experimental case study concerning a 3D-printed scaled WT blade, where regression is performed on a single observation instead of adopting the entire set of measured responses. Additionally, the suggested framework foresees the exclusion of the RTS smoother step from the GP-based algorithm for input-state estimation to allow for real-time inference. Both the simulated and the experimental applications show that a proper selection of the covariance function adopted for GP regression allows for a more accurate input estimation, which features a good accuracy even when a single response measurement is used for training the covariance function hyperparameters. Moreover, the simulated example also demonstrates that the use of smoothing can introduce accumulation errors in the input and response predictions.

Acknowledgements

The authors gratefully acknowledge the European Commission for its support of the Marie Skłodowska Curie program through the ITN DyVirt project (GA 764547).

References

- [1] AIAA Digital Engineering Integration Committee. Digital twin: Definition and value - an aiaa and aia position paper. 2020.
- [2] Kristof Maes, AW Smyth, Guido De Roeck, and Geert Lombaert. Joint input-state estimation in structural dynamics. *Mechanical Systems and Signal Processing*, 70:445–466, 2016.
- [3] Kristof Maes, Katrien Van Nimmen, E Lourens, A Rezayat, P Guillaume, Guido De Roeck, and Geert Lombaert. Verification of joint input-state estimation for force identification by means of in situ measurements on a footbridge. *Mechanical Systems and Signal Processing*, 75:245–260, 2016.

- [4] Kristof Maes, A Iliopoulos, W Weijtjens, C , and Geert Lombaert. Dynamic strain estimation for fatigue assessment of an offshore monopile wind turbine using filtering and modal expansion algorithms. *Mechanical Systems and Signal Processing*, 76:592–611, 2016.
- [5] R Cumbo, T Tamarozzi, K Janssens, and W Desmet. Kalman-based load identification and full-field estimation analysis on industrial test case. *Mechanical Systems and Signal Processing*, 117:771–785, 2019.
- [6] Frank Naets, Javier Cuadrado, and Wim Desmet. Stable force identification in structural dynamics using kalman filtering and dummy-measurements. *Mechanical Systems and Signal Processing*, 50:235–248, 2015.
- [7] Saeed Eftekhar Azam, Eleni Chatzi, Costas Papadimitriou, and Andrew Smyth. Experimental validation of the kalman-type filters for online and real-time state and input estimation. *Journal of vibration and control*, 23(15):2494–2519, 2017.
- [8] E Lourens, Costas Papadimitriou, Steven Gillijns, Edwin Reynders, Guido De Roeck, and Geert Lombaert. Joint input-response estimation for structural systems based on reduced-order models and vibration data from a limited number of sensors. *Mechanical Systems and Signal Processing*, 29:310–327, 2012.
- [9] Sofia Puerto Tchemodanova, Masoud Sanayei, Babak Moaveni, Konstantinos Tatsis, and Eleni Chatzi. Strain predictions at unmeasured locations of a substructure using sparse response-only vibration measurements. *Journal of Civil Structural Health Monitoring*, 11(4):1113–1136, 2021.
- [10] Tommaso Tamarozzi, Enrico Risaliti, Ward Rottiers, Wim Desmet, et al. Noise, ill-conditioning and sensor placement analysis for force estimation through virtual sensing. In *In International Conference on Noise and Vibration Engineering (ISMA2016)*, pages 1741–1756. KATHOLIEKE UNIV LEUVEN, DEPT WERKTUIGKUNDE, 2016.
- [11] Marius Tarpø, Bruna Nabuco, Christos Georgakis, and Rune Brincker. Expansion of experimental mode shape from operational modal analysis and virtual sensing for fatigue analysis using the modal expansion method. *International Journal of Fatigue*, 130:105280, 2020.
- [12] Peter Avitabile and Pawan Pingle. Prediction of full field dynamic strain from limited sets of measured data. *Shock and vibration*, 19(5):765–785, 2012.
- [13] Alexandros Iliopoulos, Rasoul Shirzadeh, Wout Weijtjens, Patrick Guillaume, Danny Van Hemelrijck, and Christof Devriendt. A modal decomposition and expansion approach for prediction of dynamic responses on a monopile offshore wind turbine using a limited number of vibration sensors. *Mechanical Systems and Signal Processing*, 68:84–104, 2016.
- [14] Vasilis K Dertimanis, EN Chatzi, S Eftekhar Azam, and Costas Papadimitriou. Input-state-parameter estimation of structural systems from limited output information. *Mechanical Systems and Signal Processing*, 126:711–746, 2019.
- [15] Costas Papadimitriou, Claus-Peter Fritzen, Peter Kraemer, and Evangelos Ntotsios. Fatigue predictions in entire body of metallic structures from a limited number of vibration sensors using kalman filtering. *Structural Control and Health Monitoring*, 18(5):554–573, 2011.
- [16] K.E. Tatsis, V.K. Dertimanis, C. Papadimitriou, E. Lourens, and E.N. Chatzi. A general substructure-based framework for input-state estimation using limited output measurements. *Mechanical Systems and Signal Processing*, 150:107223, 2021.
- [17] Konstantinos Tatsis, Vasilis Dertimanis, and Eleni Chatzi. Response prediction of systems experiencing operational and environmental variability. In *Computing in Civil Engineering 2019: Smart Cities, Sustainability, and Resilience*, pages 468–474. American Society of Civil Engineers Reston, VA, 2019.
- [18] Konstantinos E Tatsis, Vasilis K Dertimanis, and Eleni N Chatzi. Adaptive process and measurement noise identification for recursive bayesian estimation. In *Model Validation and Uncertainty Quantification, Volume 3*, pages 361–364. Springer, 2020.
- [19] Enrico Risaliti, Tommaso Tamarozzi, Martijn Vermaut, Bram Cornelis, and Wim Desmet. Multibody model based estimation of multiple loads and strain field on a vehicle suspension system. *Mechanical Systems and Signal Processing*, 123:1–25, 2019.
- [20] Eleni N Chatzi and Andrew W Smyth. The unscented kalman filter and particle filter methods for nonlinear structural system identification with non-collocated heterogeneous sensing. *Structural Control and Health Monitoring: The Official Journal of the International Association for Structural Control and Monitoring and of the European Association for the Control of Structures*, 16(1):99–123, 2009.
- [21] Stefano Mariani and Aldo Ghisi. Unscented kalman filtering for nonlinear structural dynamics. *Nonlinear Dynamics*, 49(1):131–150, 2007.
- [22] Konstantinos Tatsis, Long Wu, Paolo Tiso, and Eleni Chatzi. State estimation of geometrically non-linear systems using reduced-order models. *Life Cycle Analysis and Assessment in Civil Engineering: Towards an Integrated Vision*, pages 219–227, 2018.
- [23] E Lourens, Edwin Reynders, Guido De Roeck, Geert Degrande, and Geert Lombaert. An augmented kalman filter for force identification in structural dynamics. *Mechanical Systems and Signal Processing*, 27:446–460, 2012.
- [24] Saeed Eftekhar Azam, Eleni Chatzi, and Costas Papadimitriou. A dual kalman filter approach for state estimation via output-only acceleration measurements. *Mechanical Systems and Signal Processing*, 60:866–886, 2015.
- [25] Chien-Shu Hsieh. Optimal time-delayed joint input and state estimation for systems with unknown inputs. In *Proceedings of the 48th IEEE Conference on Decision and Control (CDC) held jointly with 2009 28th Chinese Control Conference*, pages 4426–4431. IEEE, 2009.
- [26] Chien-Shu Hsieh. Unbiased minimum-variance input and state estimation for systems with unknown inputs: A system reformation approach. *Automatica*, 84:236–240, 2017.
- [27] Kristof Maes, Steven Gillijns, and Geert Lombaert. A smoothing algorithm for joint input-state estimation in structural dynamics. *Mechanical Systems and Signal Processing*, 98:292–309, 2018.
- [28] Kristof Maes, E Lourens, Katrien Van Nimmen, Edwin Reynders, Guido De Roeck, and Geert Lombaert. Design of sensor networks for instantaneous inversion of modally reduced order models in structural dynamics. *Mechanical Systems and Signal Processing*, 52:628–644, 2015.
- [29] Roberta Cumbo, Lorenzo Mazzanti, Tommaso Tamarozzi, Pavel Jiranek, Wim Desmet, and Frank Naets. Advanced optimal sensor placement for kalman-based multiple-input estimation. *Mechanical Systems and Signal Processing*, 160:107830, 2021.
- [30] Lorenzo Mazzanti, Roberta Cumbo, Wim Desmet, Frank Naets, and Tommaso Tamarozzi. An improved optimal sensor placement strategy for kalman-based multiple-input estimation. In *Model Validation and Uncertainty Quantification, Volume 3*, pages 181–185. Springer, 2020.
- [31] Tulay Ercan and Costas Papadimitriou. Optimal sensor placement for reliable virtual sensing using modal expansion and information theory. *Sensors*, 21(10), 2021.

- [32] Tulay Ercan, Konstantinos Tatsis, Victor Flores Terrazas, Eleni Chatzi, and Costas Papadimitriou. Optimal sensor configuration design for virtual sensing in a wind turbine blade using information theory. In *Model Validation and Uncertainty Quantification, Volume 3: Proceedings of the 40th IMAC, A Conference and Exposition on Structural Dynamics 2022*, pages 67–70. Springer, 2022.
- [33] Tulay Ercan, Omid Sedehi, Lambros S Katafygiotis, and Costas Papadimitriou. Information theoretic-based optimal sensor placement for virtual sensing using augmented kalman filtering. *Mechanical Systems and Signal Processing*, 188:110031, 2023.
- [34] Simon J Julier, Jeffrey K Uhlmann, and Hugh F Durrant-Whyte. A new approach for filtering nonlinear systems. In *Proceedings of 1995 American Control Conference-ACC'95*, volume 3, pages 1628–1632. IEEE, 1995.
- [35] Simon J Julier and Jeffrey K Uhlmann. New extension of the kalman filter to nonlinear systems. In *Signal processing, sensor fusion, and target recognition VI*, volume 3068, pages 182–193. International Society for Optics and Photonics, 1997.
- [36] Behrouz Safarinejadian and Navid Vafamand. Kalman randomized joint ukf algorithm for dual estimation of states and parameters in a nonlinear system. *Journal of Electrical Engineering and Technology*, 10(3):1212–1220, 2015.
- [37] Eleni N Chatzi and Clemente Fuggini. Online correction of drift in structural identification using artificial white noise observations and an unscented kalman filter. *Smart Struct. Syst.*, 16(2):295–328, 2015.
- [38] Christopher K Williams and Carl Edward Rasmussen. *Gaussian processes for machine learning*, volume 2. MIT press Cambridge, MA, 2006.
- [39] Jouni Hartikainen and Simo Särkkä. Kalman filtering and smoothing solutions to temporal gaussian process regression models. In *2010 IEEE international workshop on machine learning for signal processing*, pages 379–384. IEEE, 2010.
- [40] Jouni Hartikainen and Simo Särkkä. Sequential inference for latent force models. *arXiv preprint arXiv:1202.3730*, 2012.
- [41] Simo Särkkä, Mauricio A Alvarez, and Neil D Lawrence. Gaussian process latent force models for learning and stochastic control of physical systems. *IEEE Transactions on Automatic Control*, 64(7):2953–2960, 2018.
- [42] Mauricio A Álvarez, David Luengo, and Neil D Lawrence. Linear latent force models using gaussian processes. *IEEE transactions on pattern analysis and machine intelligence*, 35(11):2693–705, Nov 2013.
- [43] Mauricio Alvarez, David Luengo, and Neil D Lawrence. Latent force models. In *Artificial Intelligence and Statistics*, pages 9–16. PMLR, 2009.
- [44] Rajdip Nayek, Souvik Chakraborty, and Sriram Narasimhan. A gaussian process latent force model for joint input-state estimation in linear structural systems. *Mechanical Systems and Signal Processing*, 128:497–530, 2019.
- [45] Joanna Zou, Eliz-Mari Lourens, and Alice Cicirello. Virtual sensing of subsoil strain response in monopile-based offshore wind turbines via gaussian process latent force models. *arXiv preprint arXiv:2207.05901*, 2022.
- [46] TJ Rogers, K Worden, and EJ Cross. On the application of gaussian process latent force models for joint input-state-parameter estimation: With a view to bayesian operational identification. *Mechanical Systems and Signal Processing*, 140:106580, 2020.
- [47] Luca Marino and Alice Cicirello. A switching gaussian process latent force model for the identification of mechanical systems with a discontinuous nonlinearity. *arXiv preprint arXiv:2303.03858*, 2023.
- [48] Konstantinos Tatsis, Vasilis K Dertimanis, Timothy J Rogers, Elizabeth Cross, Keith Worden, and Eleni Chatzi. A spatiotemporal dual kalman filter for the estimation of states and distributed inputs in dynamical systems. *Proceedings of ISMA-USD 2020*, pages 3591–3597, 2020.
- [49] Roy R Craig Jr. A review of time-domain and frequency-domain component mode synthesis method. 1985.
- [50] S. Vettori, E. Di Lorenzo, B. Peeters, M.M. Luczak, and E. Chatzi. An adaptive-noise augmented kalman filter approach for input-state estimation in structural dynamics. *Mechanical Systems and Signal Processing*, 184:109654, 2023.
- [51] Francis Galton. Regression towards mediocrity in hereditary stature. *The Journal of the Anthropological Institute of Great Britain and Ireland*, 15:246–263, 1886.
- [52] John F Kenney and ES Keeping. Linear regression and correlation. *Mathematics of statistics*, 1:252–285, 1962.
- [53] Tong Zhang. Solving large scale linear prediction problems using stochastic gradient descent algorithms. In *Proceedings of the twenty-first international conference on Machine learning*, page 116, 2004.
- [54] T L_etc Lai, Herbert Robbins, and C Zi Wei. Strong consistency of least squares estimates in multiple regression ii. *Journal of multivariate analysis*, 9(3):343–361, 1979.
- [55] Arthur E Hoerl and Robert W Kennard. Ridge regression: Biased estimation for nonorthogonal problems. *Technometrics*, 12(1):55–67, 1970.
- [56] Fourth Edition, Athanasios Papoulis, and S Unnikrishna Pillai. Probability, random variables, and stochastic processes, 2002.
- [57] I.I. Gikhman, A.V. Skorokhod, and S. Kotz. *The Theory of Stochastic Processes: I*, volume 1 of *Classics in Mathematics*. Springer Berlin Heidelberg, 2004.
- [58] Milton Abramowitz, Irene A Stegun, and Robert H Romer. Handbook of mathematical functions with formulas, graphs, and mathematical tables, 1988.
- [59] Arno Solin and Simo Särkkä. Explicit link between periodic covariance functions and state space models. In *Artificial Intelligence and Statistics*, pages 904–912. PMLR, 2014.
- [60] Simo Särkkä et al. *Recursive Bayesian inference on stochastic differential equations*. Helsinki University of Technology, 2006.
- [61] Simo Särkkä. *Bayesian filtering and smoothing*. Number 3. Cambridge university press, 2013.
- [62] Michael L Stein. *Interpolation of spatial data: some theory for kriging*. Springer Science & Business Media, 1999.
- [63] Chris Chatfield. *The analysis of time series: an introduction*. Chapman and hall/CRC, 2003.
- [64] Morris Tenenbaum and Harry Pollard. *Ordinary differential equations: an elementary textbook for students of mathematics, engineering, and the sciences*. Courier Corporation, 1985.
- [65] Andre G Journel and Charles J Huijbregts. Mining geostatistics. 1976.
- [66] Pierre Goovaerts et al. *Geostatistics for natural resources evaluation*. Oxford University Press on Demand, 1997.
- [67] Theodoros Evgeniou and Massimiliano Pontil. Regularized multi-task learning. In *Proceedings of the tenth ACM SIGKDD international conference on Knowledge discovery and data mining*, pages 109–117, 2004.
- [68] Jay M Ver Hoef and Ronald Paul Barry. Constructing and fitting models for cokriging and multivariable spatial prediction. *Journal of Statistical Planning and Inference*, 69(2):275–294, 1998.

- [69] Phillip Boyle and Marcus Frean. Dependent gaussian processes. *Advances in neural information processing systems*, 17, 2004.
- [70] Mauricio A Alvarez and Neil D Lawrence. Computationally efficient convolved multiple output gaussian processes. *The Journal of Machine Learning Research*, 12:1459–1500, 2011.
- [71] Heorhi Brzhezinski, Silvia Vettori, Emilio Di Lorenzo, Bart Peeters, Eleni Chatzi, and Francesco Cosco. On the dynamic virtualization of a 3d-printed scaled wind turbine blade. In *Model Validation and Uncertainty Quantification, Volume 3: Proceedings of the 40th IMAC, A Conference and Exposition on Structural Dynamics 2022*, pages 31–39. Springer, 2022.